FORESTRY AND NATURAL SCIENCES

Pauli Fält

Modern optical methods for retinal imaging

Publications of the University of Eastern Finland
Dissertations in Forestry and Natural Sciences No 80

UNIVERSITY OF
EASTERN FINLAND

PAULI FÄLT

Modern optical methods for retinal imaging

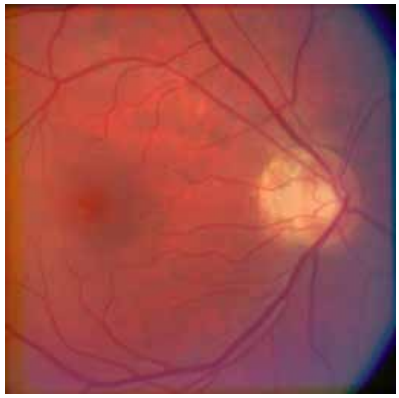

Publications of the University of Eastern Finland
Dissertations in Forestry and Natural Sciences
No 80

Academic Dissertation
To be presented by permission of the Faculty of Science and Forestry for public examination in the Louhela Auditorium in Joensuu Science Park, Joensuu, on September 14, 2012, at 12 o'clock noon.

Department of Physics and Mathematics

Kopijyvä Oy
Joensuu, 2012
Editors: Prof. Pertti Pasanen and Prof. Pekka Kilpeläinen

Distribution:
University of Eastern Finland Library / Sales of publications
P.O. Box 107, FI-80101 Joensuu, Finland
tel. +358-50-3058396
http://www.uef.fi/kirjasto

ISBN: 978-952-61-0868-1 (printed)
ISSNL: 1798-5668
ISSN: 1798-5668
ISBN: 978-952-61-0869-8 (pdf)
ISSNL: 1798-5668
ISSN: 1798-5676

Author's address:
University of Eastern Finland
Department of Physics and Mathematics
P.O.Box 111
80101 JOENSUU
FINLAND
email: pauli.falt@uef.fi

Supervisors:
Professor Markku Hauta-Kasari, Ph.D.
University of Eastern Finland
School of Computing
P.O.Box 111
80101 JOENSUU
FINLAND
email: markku.hauta-kasari@uef.fi

Professor Timo Jääskeläinen, Ph.D.
University of Eastern Finland
Department of Physics and Mathematics
P.O.Box 111
80101 JOENSUU
FINLAND
email: timo.jaaskelainen@uef.fi

Reviewers:
Professor Miika Nieminen, Ph.D.
University of Oulu
Department of Diagnostic Radiology
P.O.Box 5000
90014 OULU
FINLAND
email: miika.nieminen@oulu.fi

Professor Ela Claridge, Ph.D.
University of Birmingham
School of Computer Science
Edgbaston
BIRMINGHAM, B15 2TT
UNITED KINGDOM
email: E.Claridge@cs.bham.ac.uk

Opponent:
Professor Valery Tuchin, Ph.D.
Saratov State University
Department of Physics
83, Astrakhanskaya str.
SARATOV 410012
RUSSIA

ABSTRACT

Some medical conditions can cause damage to the retina of the eye. For example, the disease *diabetes mellitus* can cause irreversible damage to the eye, potentially leading to loss of vision or blindness. If treatment is started at an early stage, vision loss can be postponed or even prevented. In some cases, lesions and abnormal changes in the ocular fundus are the first signs of an otherwise symptomless disease. Therefore, it is important to be able to detect these early-stage changes as reliably as possible. The main aim of this thesis is to study the human eye with optical methods for the improvement of the detection of retinal changes.

In this thesis, modern optical methods for improving retinal imaging have been considered. The first method used was multispectral imaging: a commercial eye fundus camera system was modified for spectral imaging and the new system was used to measure spectral fundus images from the eyes of 72 voluntary human subjects. Of the volunteers, 55 suffered from diabetes and 17 were healthy control subjects. The second optical method was spectral-domain optical coherence tomography with adaptive optics (wavefront sensor and deformable mirrors). The system was used to measure the three-dimensional structure of the retina from the eye of a healthy human subject. Four different measurement beam sizes were used, and the respective B-scans (cross-sections of the retina) and wavefront sensor images were recorded.

It was found that the spectral information can be used to improve the visibility and contrast of the diabetic lesions in retinal images. By choosing certain spectral channel images, high-contrast pseudo-color images could be created. Also, by using spectral data, the optimal spectral power distributions of the illuminations which would maximize diabetic lesion visibility in monochrome retinal imaging were obtained. Computational example images were presented, demonstrating the potential of the optimal illuminations for diabetic lesion visibility enhancement. In the optical coherence tomography studies, it was found that with a correct choice of imag-

ing beam width, the strength of the detected signal coming from the eye could be increased. A relatively small imaging beam width (i.e. eye entrance pupil size) resulted in poor lateral imaging resolution, but increased the amount of light returning from the eye. Further analysis indicated that the optical Stiles-Crawford effect is a plausible explanation for the increase in detected intensity. The gained increase in measurement signal strength might be useful in cases where the medical condition of the eye reduces the amount of light returning from the retina (e.g. eyes with cataracts or weakly reflecting retinas).

Universal Decimal Classification: 535-1, 535-2, 535.3, 535.4, 535.8, 681.7
National Library of Medicine Classification: WN 180, WW 26, WW 141, WW 270
PACS Classification: 07.60.-j, 78.40.-q, 42.25.Hz, 42.66.Ct, 87.57.-s, 87.63.lm, 87.85.Pq
Library of Congress Subject Headings: Optics; Imaging systems; Diagnostic imaging; Eye; Retina; Fundus oculi; Spectrum analysis; Optical coherence tomography; Light filters; Reflectance; Light sources; Ophthalmology – Equipment and supplies; Diabetic retinopathy – Diagnosis
Yleinen suomalainen asiasanasto: optiikka; optiset laitteet; kuvantaminen; spektrikuvaus; optinen koherenssitomografia; silmät; verkkokalvo; diabetes – komplikaatiot

Preface

First and foremost, my deepest gratitude goes to my supervisors Prof. Markku Hauta-Kasari and Prof. Timo Jääskeläinen. I wish to thank the reviewers of my thesis, Prof. Ela Claridge and Prof. Miika Nieminen for their valuable comments and suggestions. I'm also deeply grateful to Prof. Jussi Parkkinen and Prof. Pasi Vahimaa for all their support and guidance.

I wish to acknowledge my colleagues, whom I've had the pleasure of working with during my doctoral studies: Jouni Hiltunen, Jussi Kinnunen, Ville Heikkinen, Tapani Hirvonen, Paras Pant, Jukka Antikainen, Oili Kohonen, Tuija Jetsu, Jarkko Mutanen, Juha Lehtonen, Hannu Laamanen, Joni Orava, Robert Zawadzki, Lim Yi Heng and Jakub Czajkowski. And, of course, a huge thank you to all the past and present members of the Color Research Group of the University of Eastern Finland.

This thesis would not have been possible without support from Kuopio University Hospital, Tampere University Hospital and Lappeenranta University of Technology. I wish to thank Hannu Uusitalo, Heikki Kälviäinen, Joni Kämäräinen, Lasse Lensu, Iiris Sorri, Juhani Pietilä, Valentina Kalesnykiene and Helvi Käsnänen.

During my doctoral studies I had the privilege of visiting the Center for Optical Research and Education (CORE) at Utsunomiya University (Utsunomiya, Japan). My two visits to CORE (one year + three months) would not have been possible without the kind support of Prof. Toyohiko Yatagai. I am also extremely grateful to Assoc. Prof. Barry Cense, who so patiently introduced me to the fascinating world of optical coherence tomography. I wish to thank Prof. Yoshio Hayasaki and all the CORE students and faculty members for their help and kindness.

Also, I wish to thank Prof. Yoshiaki Yasuno, Shuichi Makita and all the members of the Computational Optics Group (COG) of the University of Tsukuba (Tsukuba, Japan) for their kind assistance

and for letting us use their fantastic LabView code.

Thank you to the Magnus Ehrnrooth foundation for their personal grant.

Finally, I'd like to thank my parents Ulla and Tuomo, and my sister Päivi for their endless support during my many years of studies.

Joensuu August 7, 2012 *Pauli Fält*

ABBREVIATIONS

2-D	Two-Dimensional
3-D	Three-Dimensional
ANSI	American National Standards Institute
AO	Adaptive Optics
AOTF	Acousto-Optic Tunable Filter
CCD	Charge Coupled Device
CIE	Commission Internationale de l'Eclairage
DM	Deformable Mirror
FCS	Fundus Camera System
FWHM	Full Width at Half Maximum
GDB-ICP	Generalized Dual-Bootstrap Iterative Closest Point
ICNIRP	International Commission on Non-Ionizing Radiation Protection
IR	InfraRed
LCTF	Liquid Crystal Tunable Filter
NIR	Near-InfraRed
OCT	Optical Coherence Tomography
PSO	Particle Swarm Optimization
RGB	Red/Green/Blue (color channels)
SCE	Stiles-Crawford Effect
SD	Spectral-Domain
SPD	Spectral Power Distribution
TD	Time-Domain
UV	UltraViolet
WFS	WaveFront Sensor

LIST OF PUBLICATIONS

This thesis consists of the present review of the author's work in the fields of spectral color science and optical coherence tomography, and the following selection of the author's publications:

I P. Fält, J. Hiltunen, M. Hauta-Kasari, I. Sorri, V. Kalesnykiene, and H. Uusitalo,"Extending diabetic retinopathy imaging from color to spectra," in *Proceedings of SCIA'09 – 16th Scandinavian Conference on Image Analysis, Lecture Notes in Computer Science (LNCS),* **5575,** 149–158 (2009).

II P. Fält, J. Hiltunen, M. Hauta-Kasari, I. Sorri, V. Kalesnykiene, J. Pietilä, and H. Uusitalo, "Spectral imaging of the human retina and computationally determined optimal illuminants for diabetic retinopathy lesion detection," *Journal of Imaging Science and Technology* **55**(3), 030509-1–030509-10 (2011).

III P. Fält, R. J. Zawadzki, and B. Cense, "The effect of collimator lenses on the performance of an optical coherence tomography system," in *Proceedings of SPIE Photonics West 2011, Ophthalmic Technologies XXI, San Francisco, USA, January 22-24,* **7885,** 78850X (2011).

IV P. Fält, R. J. Zawadzki, and B. Cense, "Influence of imaging beam size and Stiles-Crawford effect on image intensity in ophthalmic adaptive optics - optical coherence tomography," *Optics Letters*, 2012 (submitted).

Throughout the overview, these papers will be referred to by Roman numerals. These original papers have been included at the end of this thesis with the permission of the publishers.

AUTHOR'S CONTRIBUTION

The publications selected in this dissertation are original research papers on spectral imaging and optical coherence tomography of the human retina.

In Papers **I** and **II**, the original idea of modifying a commercial eye fundus camera system for spectral imaging originated from Prof. Joni Kämäräinen and Dr. Lasse Lensu (Lappeenranta University of Technology, Finland).

In Paper **I**, the modifications to the fundus camera system were done by Dr. Jouni Hiltunen and the author. All retinal measurements were done by the author with the assistance of the co-authors. All data analysis and all numerical computations were done by the author.

In Paper **II**, the modifications to the fundus camera system were done by Dr. Jouni Hiltunen and the author. All retinal measurements were done by the author with the assistance of the co-authors. All data analysis and all numerical computations were done by the author. The original idea and method of calculating the optimal illuminations was the author's.

In Paper **III**, all data analysis, all numerical computations and all optical modeling using ZEMAX software were done by the author.

In Paper **IV**, all data analysis and all numerical computations were done by the author.

The author has written the manuscripts to each of the Papers, **I**–**IV**. The introduction in Paper **II** was written by the author together with the co-authors.

Contents

1 INTRODUCTION **1**

2 RESEARCH PROBLEMS ADDRESSED IN THIS THESIS **5**

3 THEORY **7**
3.1 Spectral color theory 7
3.2 Spectral measurement methods 10
3.3 Retina and diabetes 15
3.3.1 Structure of the human eye 15
3.3.2 Stiles-Crawford effect 17
3.3.3 Diabetic retinopathy 18
3.4 Spectral fundus imaging 21
3.5 Particle swarm optimization 24
3.6 Optical coherence tomography 26

4 EXPERIMENTAL STUDIES AND RESULTS **33**
4.1 Spectral imaging of the ocular fundus 33
4.2 Spectral fundus images and pseudo-color images . . 33
4.3 Calculation of optimal illuminations for diabetic retinopathy lesion detection 35
4.4 Optimal illuminations and computational example images 37
4.5 Effect of the collimator lens in the sample arm of an optical coherence tomography system 40
4.6 Influence of beam size and SCE on image intensity in adaptive optics optical coherence tomography 44

5 DISCUSSION **49**

REFERENCES **53**

APPENDIX: ORIGINAL PUBLICATIONS **65**

1 Introduction

The bottom of the eye, the retina, can reflect a person's medical condition. In addition to eye diseases such as glaucoma, macular degeneration and retinal tumors, changes in the visual appearance of the retina can also indicate increased intracranial pressure or the presence of *diabetes mellitus* [1–7]. Diabetes is a chronic disease that disrupts the normal glucose metabolism in the body and can cause a wide spectrum of medical complications [8]. In Type 1 diabetes, the body's own immune system destroys the insulin-producing beta cells of the pancreas, leading to a state where the body's cells cannot absorb glucose from the blood. Glucose remains in the blood, causing occlusion of thin blood vessels, potentially damaging the peripheral nervous system, kidneys and other parts of the body. Untreated diabetes can lead to loss of consciousness, coma and even death. Diabetes-related complications can lead to expensive medical treatments, surgeries or even amputations.

In the most common type of diabetes, Type 2, the insulin resistance of the body's cells is increased, which leads to the same situation as in Type 1. Type 2 diabetes is strongly associated with overweight and obesity [9]. In just a couple decades, Type 2 diabetes has grown into a global epidemic. In Finland, there were approximately 300,000 people diagnosed with diabetes in 2009 and it was estimated that 200,000 Finns had the disease without being aware of it [10, 11]. This means that 10% of the entire Finnish population had diabetes in 2009, a number which has undoubtedly increased since. The treatment of diabetes and its complications requires expensive medicines, expensive equipment, and highly-trained health care professionals. Diabetes lowers the quality of life of the patients and causes large costs to the society.

If diabetes can be detected at an early stage, a large number of medical complications can be avoided or at least postponed. What makes diabetes especially problematic is that it's often symptomless

until a certain degree of damage has already happened. Amongst other parts of the body, diabetes also causes damage to the retina (i.e. diabetic retinopathy). Sometimes these abnormal changes in the bottom of the eye, and the related vision problems, are the first indication of the presence of diabetes. Therefore, it is very important to be able to detect these retinal changes, so that treatment and follow-ups can be started in as early a stage as possible.

Modern optical measurement methods can offer safe, non-destructive, non-contact approaches to the observation of the retina and its structures. The first optical method considered in this thesis is *spectral imaging* [12]. Unlike in conventional 1-channel monochrome imaging or 3-channel RGB color imaging, in spectral imaging, one captures information from several, tens or even hundreds of individual channels from adjacent wavelength regions of the electromagnetic spectrum. Spectral imaging allows one to study and exploit the wavelength-dependent optical characteristics of the object in a way that would not be possible with, e.g., standard RGB imaging.

The second optical method used in this thesis is *optical coherence tomography* (OCT) [13,14]. OCT is an interferometric method which allows one to obtain the three-dimensional structure of an optically scattering medium, e.g. paper, skin, blood vessels, teeth, the anterior segment of the eye or the retina [15–23]. Two different approaches to OCT are time-domain OCT and Fourier-domain OCT, which includes swept source OCT and spectral-domain OCT. In the thesis work, the method used was spectral-domain OCT with adaptive optics. Adaptive optics (a wavefront sensor and deformable mirrors) were used to correct for the optical aberrations created by the optics of the eye [24–27].

In the sample arm of an optical-fiber-based OCT system, the first free-space optical element is the lens that collimates the beam emerging from the fiber. In this thesis, it is shown that the selection of the focal length of this collimator lens has an effect on detected intensity in OCT scans of the human retina. This is found to be connected to the optical Stiles-Crawford effect (directional reflection

from the retina). The increase in detected intensity (at the cost of lateral imaging resolution) might be useful when doing OCT scans of the retina in challenging cases (e.g. weakly reflecting retinas or eyes with cataracts).

The thesis is organized as follows: first, the main aims of this thesis and how they were addressed are listed in Chapter 2. Chapter 3 gives a brief introduction to spectral color theory and the most typical spectral measurement methods, followed by a description of the basic structure of the human eye, the Stiles-Crawford effect and diabetic retinopathy. The spectral fundus imaging is discussed in Section 3.4. The theories behind particle swarm optimization and OCT are introduced in Sections 3.5 and 3.6, respectively. Chapter 4 describes the work done in Papers **I**–**IV**. Finally, the main claims and findings of this thesis are discussed in Chapter 5.

2 Research problems addressed in this thesis

The main aims of the thesis work and how they were addressed are as follows:

1. To construct an optical device for the spectral imaging of the human retina.

   ⇒ *A spectral fundus camera system was constructed from a commercial ophthalmic eye fundus camera.*

2. To gather a database of spectral fundus images from diabetic and healthy eyes.

   ⇒ *Spectral fundus images were measured from the eyes of 72 voluntary human subjects: 55 diabetic patients and 17 healthy subjects.*

3. To use the spectral color information to enhance the visibility of diabetic lesions in the retinal images.

   ⇒ *Spectral channel images were used to create pseudo-color fundus images with enhanced visibility of diabetic lesions.*

4. To use the spectral color information to obtain the optimal spectral power distributions of the illuminations which maximize the contrast and visibility of diabetic lesions in retinal imaging.

   ⇒ *Using the spectral information and the particle swarm optimization algorithm, the optimal spectral power distributions of the illu-*

minations for detection of different diabetic lesions were calculated. Computational example images of the performance of the optimal illuminations were presented.

5. To show that the focal length of the first collimator lens in the sample arm of an adaptive optics optical coherence tomography (AO-OCT) system affects the detected intensity in retinal scans.

   ⇒ *Using a spectral-domain AO-OCT system, the effects of four different collimator lenses on the detected intensity in retinal imaging were tested. Retinal cross-sections (B-scans) and wavefront sensor images were recorded for each collimator lens separately.*

6. To show that in AO-OCT, the eye entrance pupil size has an effect on the amount of light returning from the eye via the optical Stiles-Crawford effect (directional reflection from the retina).

   ⇒ *Based on measured B-scans and wavefront sensor images, it was shown that the focal length of the collimator lens affects the eye entrance pupil size, the spot size on the retina (lateral imaging resolution), the contribution of the optical Stiles-Crawford effect on the light returning from the eye, and the spot size on the tip of the optical fiber which guides the reflected light to the detection arm. By selecting the focal length of the collimator lens correctly, the intensity of the detected signal coming from the eye can be increased at the cost of some lateral imaging resolution.*

3 Theory

3.1 SPECTRAL COLOR THEORY

Electromagnetic radiation consists of energy quanta called *photons* [28, 29]. The energy E of a photon is inversely proportional to its wavelength λ according to a well-known formula: $E = hc/\lambda$, where $h = 6.62606957 \times 10^{-34}$ J·s is Planck's constant and $c = 299792458$ m/s is the speed of light in a vacuum. As the wavelength of a photon decreases, its energy increases, as can be seen from Fig. 3.1. Electromagnetic radiation can be classified into groups according to wavelength: radio waves have the lowest energies and longest wavelengths, ranging roughly from 10 cm to 100,000 km. At the other end of the spectrum, gamma rays have very high energies and picometer-scale wavelengths.

The human eye is sensitive only to a relatively narrow band of wavelengths from 380 nm to 780 nm (1 nm = 10^{-9} m) [28, 29]. This wavelength band is called *the visual range of light* or *the visible spectrum*. The wavelength limits 380 nm and 780 nm are not strict; the range 380–400 nm also belongs to the ultraviolet-A (UV-A) region and 700–780 nm also belongs to the near-infrared (NIR) region. It is also common for other adjacent classes of electromagnetic radiation to overlap. When the photoreceptors of the eye (rods and cones) detect radiation from the visual range of light, signals are sent to the visual cortex of the brain and sensations of *vision* and *color* are produced. Different wavelengths in the range 380–780 nm correspond to different colors, as shown by the color spectrum in Fig. 3.1.

Visual observation always consists of three elements: illumination, object and observer as presented in Fig. 3.2. The object is illuminated by light which has a spectral distribution $S(\lambda)$ as a function of wavelength. The object itself reflects a certain percentage of photons at each wavelength; this wavelength-dependent optical property is called *reflectance* $R(\lambda)$. If $R(\lambda_1) = 1$ (i.e. 100%), then the

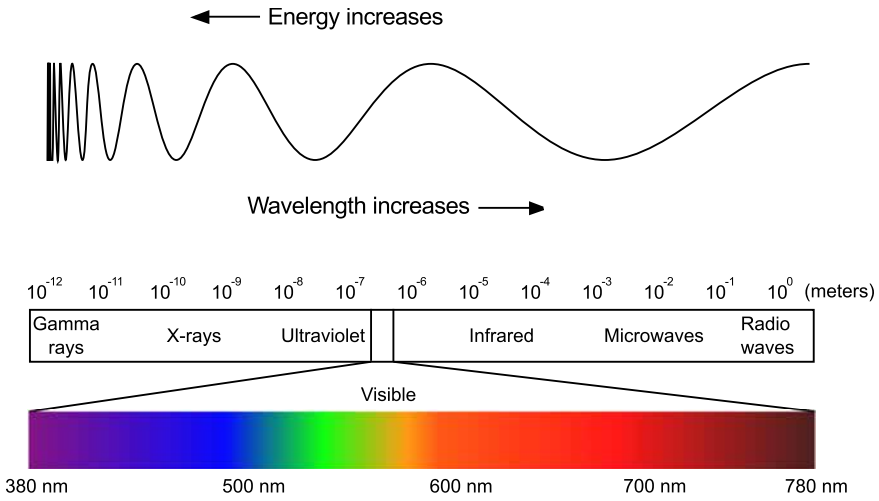

Figure 3.1: The electromagnetic spectrum. The relation between photon wavelength and energy, and the wavelength-regions of electromagnetic radiation are shown.

object reflects all of the incident photons with a wavelength of λ_1. Analogously, if $R(\lambda_2) = 0$ (i.e. 0%), the object absorbs or transmits all of the photons with wavelength λ_2, but reflects none of them. Finally, the reflected light is detected by an observer (e.g. a human, an animal or a camera) which has one, or several, detectors with different spectral sensitivities. For example, a human observer has three classes of detectors (photoreceptors) responsible for color vision, i.e. L-, M- and S-cones, which detect long, medium and short wavelengths, respectively (see Fig. 3.2).

Reflectance is independent of illumination or observer, and therefore it is the most accurate way to present the color of an object. In color-related applications, it is desirable to obtain reflectance data from an object, as it enables one to calculate, e.g., standard color coordinates, optimal spectral filters or the detected signal for any arbitrary observer in any illumination.

If a point (x, y) on the object's surface has reflectance $R(x, y; \lambda)$, then the detected signal $v_i(x, y)$ from this point is [28, 30]:

$$v_i(x, y) = \int_0^\infty S(\lambda) R(x, y; \lambda) H_i(\lambda) \mathrm{d}\lambda + v_{i,\mathrm{dark}} \,, \tag{3.1}$$

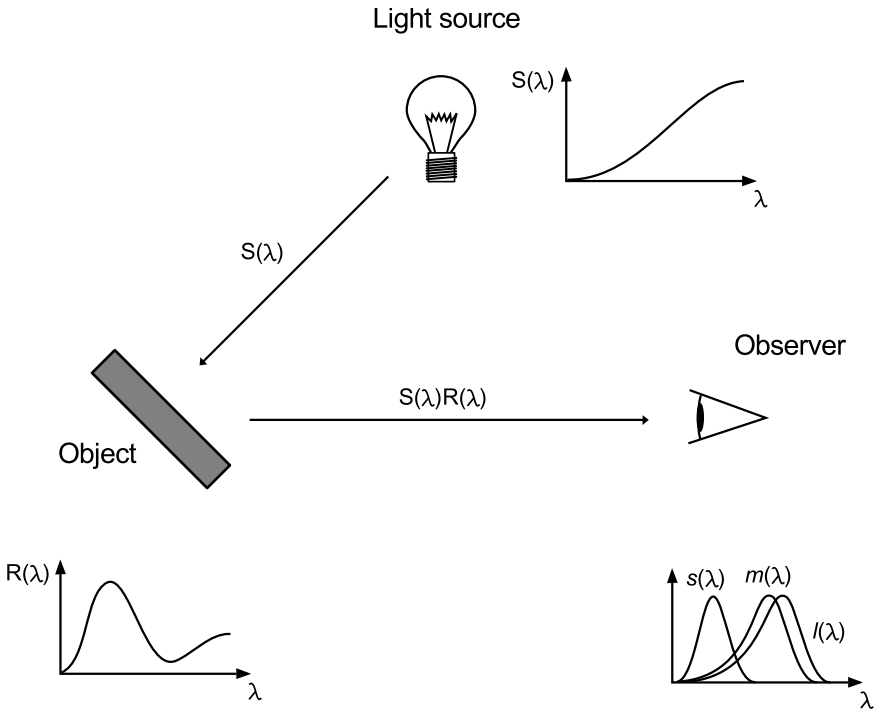

Figure 3.2: The trinity of illumination, object and observer. Here, $S(\lambda)$ is the spectral distribution of light emitted by the light source, $R(\lambda)$ is the spectral reflectance of the (uniform) object, and $l(\lambda)$, $m(\lambda)$ and $s(\lambda)$ are the human observer's spectral sensitivity functions for long, medium and short wavelengths, respectively.

where $S(\lambda)$ is the spectral distribution of the illumination, $H_i(\lambda)$ is the spectral sensitivity function of the observer's i^{th} detector and $v_{i,\text{dark}}$ is the measured dark noise for the i^{th} detector.

In practice, all of the functions are considered to be discrete n-dimensional vectors within a certain wavelength range, i.e., $S(\lambda)$, $R(x, y; \lambda)$ and $H_i(\lambda)$ become column-vectors $\mathbf{s}, \mathbf{r}, \mathbf{h}_i \in \Re^n$, respectively. For example, reflectance

$$\mathbf{r} = [R(x, y, \lambda_1), R(x, y, \lambda_2), \ldots, R(x, y, \lambda_n)]^{\mathrm{T}} , \tag{3.2}$$

where T denotes transpose. Now Eq. (3.1) can be written in matrix notation as

$$v_i(x,y) = \mathbf{w}_i^{\mathrm{T}}\mathbf{r} + v_{i,\mathrm{dark}} \ , \tag{3.3}$$

where the vector

$$\mathbf{w}_i = \mathrm{diag}(\mathbf{s})\mathbf{h}_i \tag{3.4}$$

describes the combined spectral effect of the illumination and the i^{th} detector.

If the observer has m spectrally unique detectors, one gets m values for point (x,y). One can now define a vector $\mathbf{v} \in \Re^m$ which contains the m detected values $v_i(x,y)$, $i = 1,\ldots,m$, as follows:

$$\mathbf{v} = \mathbf{W}^{\mathrm{T}}\mathbf{r} + \mathbf{v}_{\mathrm{dark}} \ , \tag{3.5}$$

where the $n \times m$ matrix $\mathbf{W}$ has the vectors $\mathbf{w}_i$ on its columns, and vector $\mathbf{v}_{\mathrm{dark}} \in \Re^m$ contains the measured dark noise values $v_{\mathrm{i,dark}}$. If measurements are also made from a perfectly reflecting white reference sample, for which the reflectance is $R_{\mathrm{white}}(\lambda) = 1$ within the wavelength range of interest, one gets

$$\mathbf{v}_{\mathrm{white}} = \mathbf{W}^{\mathrm{T}}\mathbf{r}_{\mathrm{white}} + \mathbf{v}_{\mathrm{dark}} \ . \tag{3.6}$$

Now, one can calculate reflectance as the ratio of the measured sample spectrum and the white reference spectrum:

$$\mathbf{r} = \frac{\mathbf{v} - \mathbf{v}_{\mathrm{dark}}}{\mathbf{v}_{\mathrm{white}} - \mathbf{v}_{\mathrm{dark}}} \ . \tag{3.7}$$

Different methods for measuring the above spectra are discussed in Section 3.2.

3.2 SPECTRAL MEASUREMENT METHODS

Figures 3.3, 3.4 and 3.5 represent the typical methods for spectral measurements and imaging: point measurements, line scanning measurements and wavelength scanning imaging, respectively. Point measurement devices, like typical spectrometers, observe light coming from a relatively small area on the object. A dispersive element,

such as a prism or a diffractive grating, disperses the incoming light into its spectral components, and the spectrum is focused onto a detector array.

A line spectral camera works in similar fashion, but instead of a single point, the spectra of the light coming from all of the points along a line are recorded by a two-dimensional (2-D) detector array. As shown in Fig. 3.4, the light coming from the sample is guided through a narrow slit, dispersed into its spectral components by a prism-grating-prism component, and focused onto the 2-D detector [31]. In order to record a full spectral image, the measurement line must be scanned on the two-dimensional surface of the object, by moving either the object or the line spectral camera. All of the spectra from each line are recorded and a spectral image is constructed in subsequent data processing.

Whereas the point and line measurement devices measure the electromagnetic spectra directly and require spatial scanning for spectral image acquisition, the wavelength scanning camera actually records an image similarly to a standard monochrome grayscale camera, except that the images are captured through a collection of optical bandpass filters. A grayscale image of the object is captured for every filter individually, and a spectral image is formed by "stacking" the images in wavelength order into a three-dimensional matrix, which now has two spatial dimensions and every spatial pixel contains a spectrum along the third dimension. Wavelength scanning is typically done with narrow bandpass interference filters, a liquid crystal tunable filter (LCTF) or an acousto-optic tunable filter (AOTF) [32, 33]. In the case of the wavelength scanning camera, the optical bandpass filtering can also be done by filtering the light source and illuminating the object with filtered light. No bandpass filtering is required between the object and the detector in this case.

The detector's spectral sensitivity functions (a.k.a. quantum efficiency functions) can be interpreted as spectral filters which allow certain amounts of each wavelength to pass. In Fig. 3.6, the spectral sensitivity functions for red, green and blue (RGB) chan-

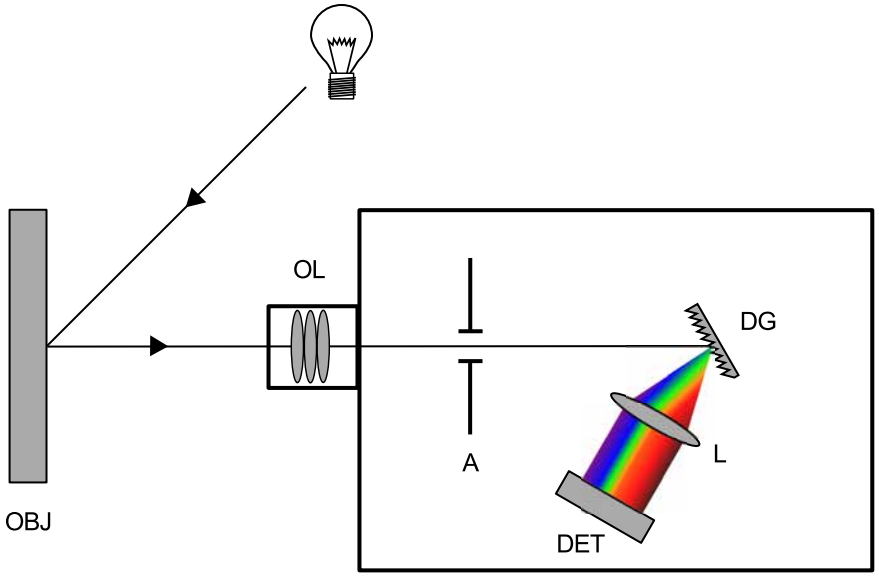

Figure 3.3: Spectral point measurement device. The device measures a spectrum from a single point on the object. OBJ: object; OL: objective lens; A: aperture; DG: diffractive grating; L: lens; DET: detector.

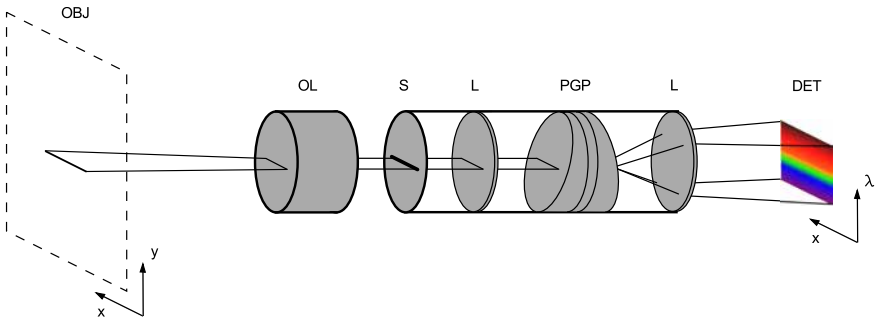

Figure 3.4: Line measuring spectral camera. The spectral camera records all spectra from a single line on the object. OBJ: object; OL: objective lens; S: slit; L: lens; PGP: prism-grating-prism component; DET: detector.

nels of a commercial Canon 10D (Canon, Inc., Japan) color camera are shown. The sensitivity functions of RGB cameras typically attempt to mimic human perception in order to make the color appearance of the captured images match a human observer's opin-

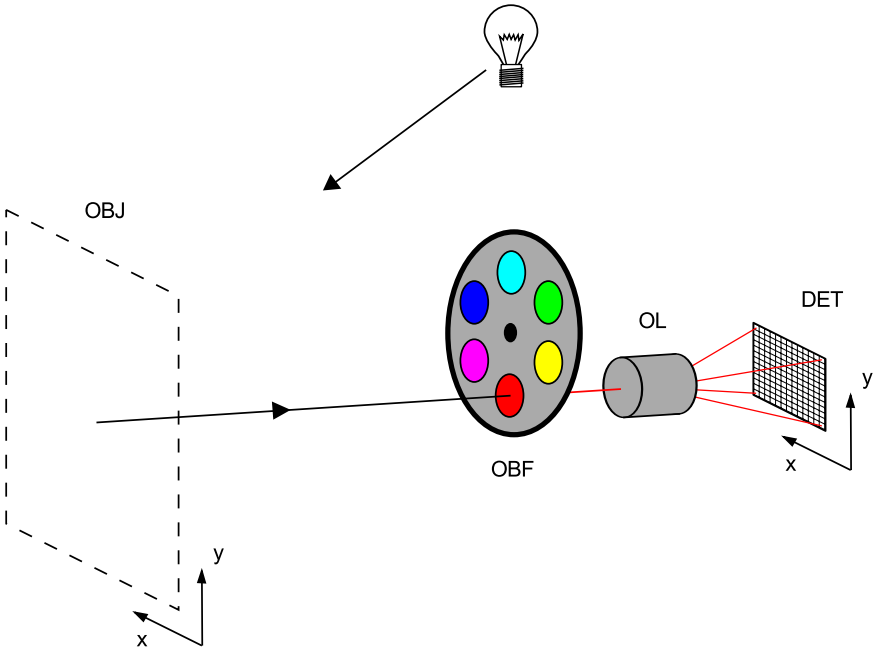

Figure 3.5: Wavelength scanning spectral camera. The spectral camera records a two-dimensional grayscale image of the object for each optical bandpass filter. OBJ: object; OBF: optical bandpass filter; OL: objective lens; DET: detector.

ion of the scene as well as possible [34]. However, since the R(λ), G(λ) and B(λ) sensitivity functions have relatively broad optical bandwidths, and because the detector integrates all the spectral information within a band into a single value, a large amount of wavelength-dependent information is lost.

For comparison, the spectral transmittances of 30 narrow bandpass interference filters are shown in Fig. 3.7. These filters also span the visual range of light, but unlike in the case of only three filters (R, G and B), the whole spectral range is now sampled in much finer detail. Instead of just R, G and B values, a spectral camera incorporating all of the narrow bandpass filters returns 30 wavelength-dependent values for each pixel.

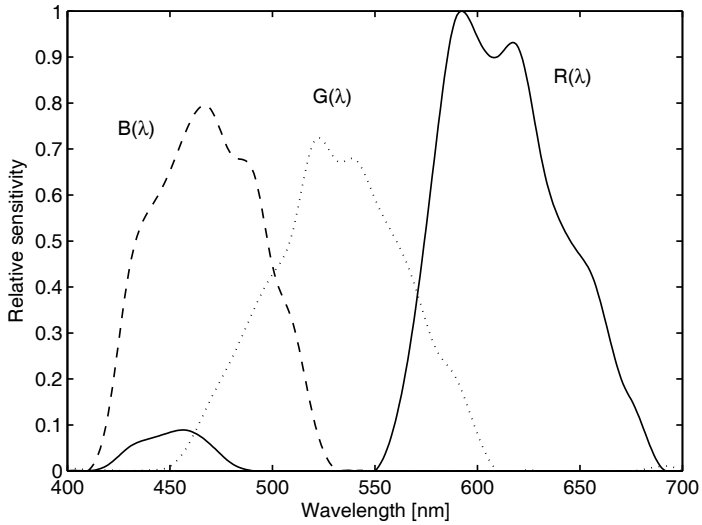

Figure 3.6: Spectral sensitivity functions of a commercial Canon 10D camera. Here, R(λ), G(λ) and B(λ) are the spectral sensitivity functions for the red, green and blue channel, respectively.

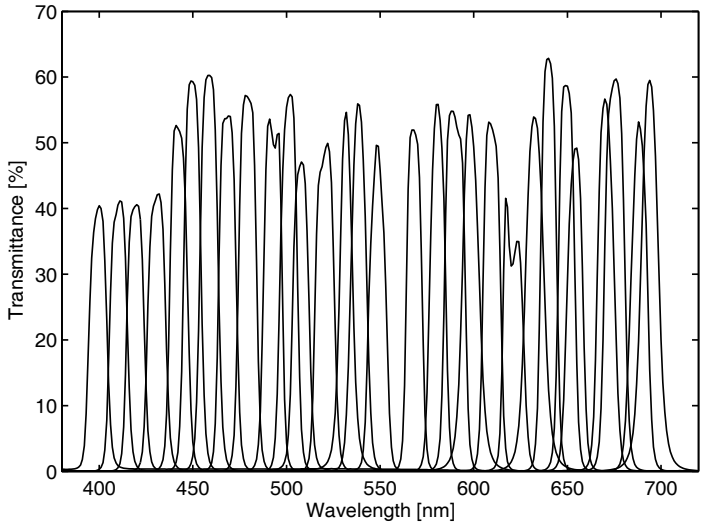

Figure 3.7: Spectral transmittances of 30 narrow bandpass interference filters.

3.3 RETINA AND DIABETES

3.3.1 Structure of the human eye

The simplified structure of the human eye is presented in Fig. 3.8(a). Light enters the eye through the transparent *cornea*, which transmits over 99% of the visible light [35]. The cornea is a significant refractive element in the optical system of the eye with a refractive index of $n = 1.376$ at 555 nm [36]. Light passes through the anterior segment which is filled with a transparent and colorless liquid called the *aqueous humor* ($n = 1.336$, [36]). The *iris* adaptively adjusts the size of the *pupil* and thus controls the amount of light that can reach the bottom of the eye. The eye bottom is also called the *ocular fundus*. The elastic *crystalline lens* focuses the incident light on the photoreceptors of the retina. The refractive index inside the lens varies and has an average value of $n = 1.408$ [37]. The *vitreous humor* is transparent gel which fills the posterior cavity of the eye. The vitreous humor is over 99% water and contains very small amounts of solids (collagen fibrils, hyaluronic acid, glucose, etc.) [38]. Still, the vitreous forms a gelatinous substance with a refractive index of $n = 1.336$ [36].

Between the vitreous and the hard outer shell of the eye (*sclera*) lie the *retina* and the *choroid*. The retina is a complex multilayered structure which contains the photosensitive elements of the eye (rods and cones) and the neural network that preprocesses the visual information and transmits it to the visual cortex of the brain via nerve fibers (*optic nerve*). The retina has an average thickness of $\sim$250 μm, and it is estimated to have an average refractive index of $n = 1.36$ [40–42]. The retina can be segmented into the following layers [28, 34, 43]: inner limiting membrane, nerve fiber layer, ganglion cell layer, inner plexiform layer, inner nuclear layer, outer plexiform layer, outer nuclear layer, outer limiting membrane, photoreceptor layer and retinal pigment epithelium (RPE). These layers are shown in Fig. 3.9. Bruch's membrane divides the retina and the choroid into their own segments. The choroid contains a large concentration of blood vessels. The choroid and the RPE contain a

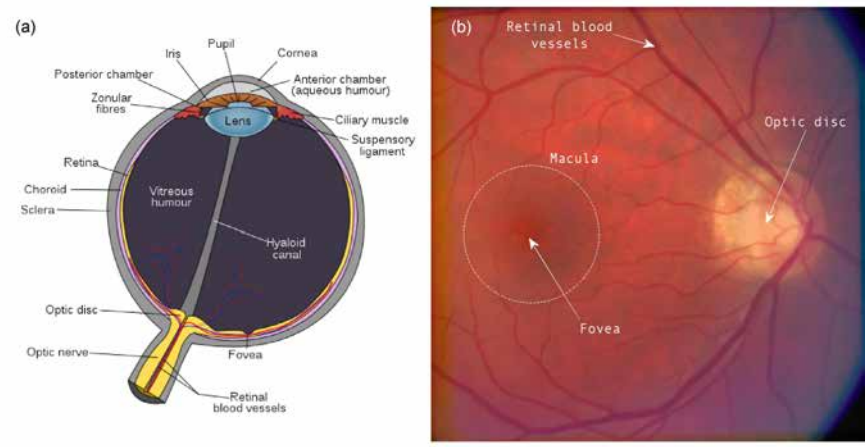

Figure 3.8: Structure of the human eye: (a) simplified cross-section of the human eye (source: public domain, [39]), and (b) an image of the bottom of the eye, i.e. ocular fundus.

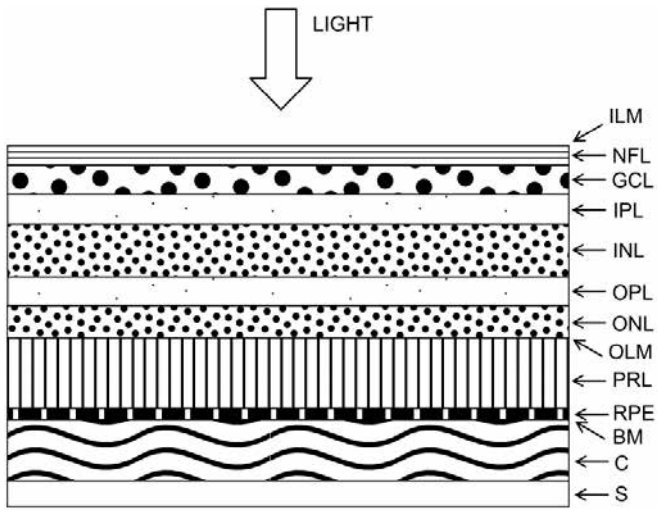

Figure 3.9: Simplified cross-section of the retina, choroid and sclera. ILM: inner limiting membrane; NFL: nerve fiber layer; GCL: ganglion cell layer; IPL: inner plexiform layer; INL: inner nuclear layer; OPL: outer plexiform layer; ONL: outer nuclear layer; OLM: outer limiting membrane; PRL: photoreceptor layer; RPE: retinal pigment epithelium; BM: Bruch's membrane; C: choroid; S: sclera.

photoprotective pigment called *melanin*, which has a strong effect on the reflectance spectrum [44–46].

Figure 3.8(b) is an image taken of the ocular fundus of a healthy human eye. The *macula* is the region of sharp central vision and it has the highest concentration of cone photoreceptors in the retina. On average, there are approximately 8 million cones and 120 million rods in the human retina [47]. The *fovea*, or the foveal pit, at the center of the macula, has only cones and no rods. The *optic disc*, also known as the blind spot, is the visible part of the optic nerve which contains no photoreceptors.

3.3.2 Stiles-Crawford effect

It is well known that photons entering the eye near the center of the pupil produce a stronger sensation of brightness than they would if they entered the eye near the edge of the pupil. This phenomenon is known as the *psychophysical* Stiles-Crawford effect (SCE) and is caused by the directional sensitivity of the cone photoreceptors [28, 48–50]. Cones do not absorb photons arriving from arbitrary directions, but instead they have relatively small acceptance angles. In this respect, cones behave like optical fibers. Therefore, due to the orientation of the cones, the photons coming from the center of the pupil have a higher chance of being absorbed by the photoreceptors. Photons coming from the edges of the pupil arrive at the retina at steeper angles and may be scattered rather than absorbed.

The so-called *optical* SCE is also caused by the waveguiding property of the cones. In optical SCE, the photoreceptors guide the reflected light from the retina more towards the center of the pupil than towards the edges [51, 52]. The effect of the optical SCE on the detected intensity in adaptive optics optical coherence tomography is discussed in Section 4.6 and Paper **IV**.

3.3.3 Diabetic retinopathy

Diabetes mellitus is a chronic disease that causes hyperglycemia, i.e. high levels of glucose (sugar) in the blood [8]. Beta cells in the pancreas produce a hormone called *insulin*, which controls the blood glucose levels. Most cells in the body require insulin to absorb glucose from the blood. In Type 1 diabetes, the beta cells are destroyed by the body's own immune system, which leads to low insulin levels and hyperglycemia. In Type 2 diabetes, insulin production may be only partially damaged, but the insulin resistance of the body's cells is increased. This means that cells don't necessarily respond to normal levels of insulin anymore, which again leads to hyperglycemia. Type 2 diabetes is often associated with obesity and metabolic syndrome. Gestational diabetes differs from Types 1 and 2 as it appears only in pregnant women. After the pregnancy, the diabetes may or may not disappear. Even in the former case, gestational diabetes is an indicator of a heightened probability of getting the disease sometime after the pregnancy. Besides the three types of diabetes mentioned above, other forms of the disease also exist. Of all the manifestations of the disease, Type 2 is the most common.

If left untreated, diabetes can cause a wide range of complications throughout the body. For example, diabetes can damage the peripheral nervous system (*diabetic neuropathy*), kidneys (*diabetic nephropathy*) and the retina of the eye (*diabetic retinopathy*). In diabetic retinopathy, typical early-stage complications in the retina include microaneurysms and small hemorrhages, generally called small red dots (see Fig. 3.10) [7,53]. Vascular leakage and swelling (edema) may appear in the retina, leaving behind yellowish-white, typically sharp-edged lipid deposits (hard exudates). Occlusion of small blood vessels leads to the creation of white, bloodless nonperfusion areas (microinfarcts, also called soft exudates or cotton wool spots due to their blurry-edged appearance). Later-stage proliferative diabetic retinopathy is characterized by abnormal changes to the vasculature of the retina, namely, neovascularization. In neo-

vascularization, the body tries to overcome oxygen deprivation by growing new blood vessels. However, as these new vessels are often thin and fragile, they break easily and bleed into the surrounding tissue. Fibrosis may also be present in varying degrees. Proliferative diabetic retinopathy can lead to serious complications, such as retinal detachment. Any lesions appearing in the macular area of the retina, or ones that obscure the macula, lead to loss of central vision. Diabetic retinopathy is one of the leading causes of blindness in the world.

Diabetes is already considered a global epidemic. In Finland alone, there were approximately 300,000 people diagnosed with either Type 1 or Type 2 diabetes in 2009 [11]. It was also estimated that 200,000 Finns had the disease, but were not aware of it. If true, then approximately 500,000 Finns (10% of the population) had diabetes in 2009. According to a study released by the Finnish National Diabetes Prevention and Treatment Development Program DEHKO, 1,304 million euros, i.e. 8.9% of all Finnish health care expenses, were used to treat diabetes and its complications in 2007 [10]. On average, from 1998 to 2007, the number of diabetes patients increased by 4.7% per year, and the health care cost increased by 6.2% per year. The same trend can be seen in many countries all over the world, and the global costs of diabetes increase year by year.

Diabetes causes damage to the body progressively over time, so the medical complications and the costs of treatment increase continuously if the disease is left undiagnosed or untreated. The standard methods of diagnosis for diabetes are the measurement of fasting plasma glucose level from venous blood and a glucose tolerance test [11]. If diabetes is diagnosed at an early stage, and treatment and regular follow-ups are started immediately, the overall quality of life of the patient can be significantly improved. Also, if expensive treatments and surgeries associated with late-stage diabetes can be postponed or avoided altogether, the costs to society are reduced. Problems arise from the fact that diabetes is often symptomless until a certain degree of damage to the body has al-

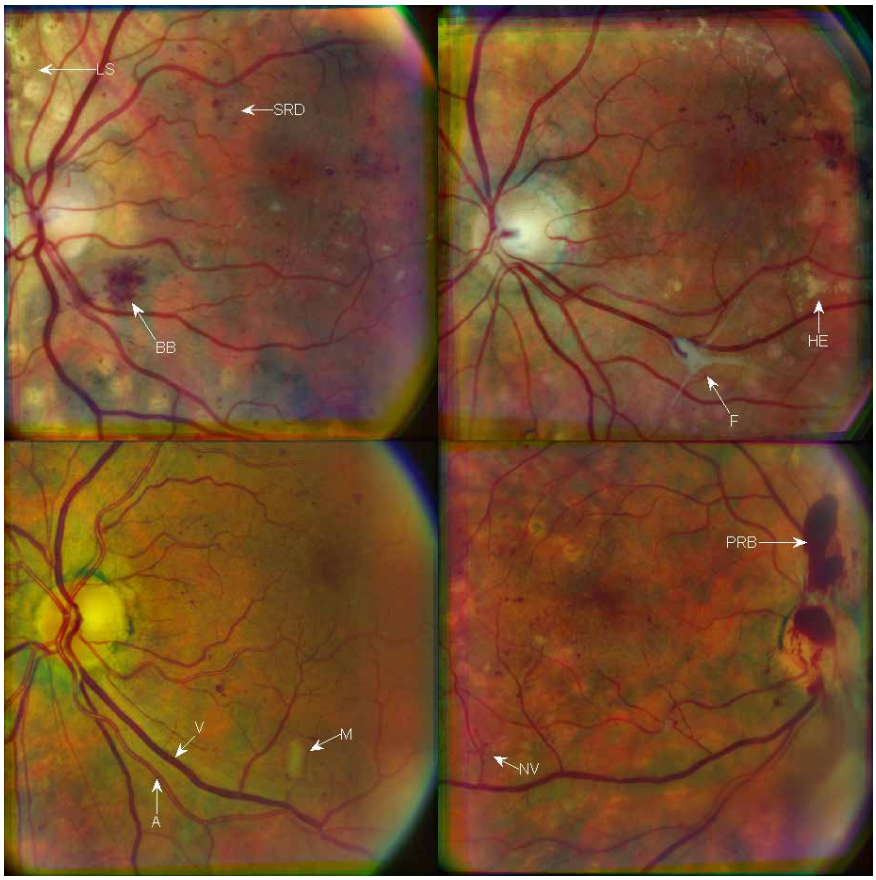

Figure 3.10: Four ocular fundi with diabetic retinopathy lesions: BB: blot bleeding; SRD: small red dots; HE: hard exudates; F: fibrosis; M: microinfarct; PRB: preretinal bleeding; NV: neovascularization. Also, laser photocoagulation scars (LS), arteries (A) and veins (V) are identified. These images are RGB representations calculated from spectral fundus images. Adaptive histogram equalization has been used for visualization reasons.

ready occurred. In some cases, vision problems caused by diabetic retinopathy are the first indication of diabetes. Therefore, developing methods for early detection of diabetic retinopathy is very important. In this thesis, one objective is to study spectral fundus imaging as an improved screening method for diabetes. The final diagnosis is always done by measuring blood plasma glucose levels as mentioned above.

3.4 SPECTRAL FUNDUS IMAGING

For eye care professionals, a *fundus camera* is a standard tool for examining the condition of the patient's retina. The working principle of a fundus camera is based on an ophthalmoscope, an optical instrument for illuminating and observing the retina, first successfully introduced in 1851 by Hermann von Helmholtz (1821–1894) [54]. A modern fundus camera system (FCS) typically consists of a Xenon flash light and an RGB camera combined with microscope optics. In addition to RGB imaging, many researchers in the past decades have performed spectral point measurements and spectral imaging of the ocular fundus [46, 55–68]. In Papers **I** and **II**, a commercial Canon CR5-45NM fundus camera (Canon, Inc., Japan) was modified for spectral imaging (Fig. 3.11). All unnecessary components, such as the original flash light source and the control electronics, were removed from the fundus camera. The camera was then modified as a wavelength scanning spectral camera system similar to Fig. 3.5, except that the spectral filtering was performed before illuminating the object (Fig. 3.12). An external Schott Fostec DCR III light box with a halogen lamp and a daylight-simulation filter was used as a broadband light source. The optical bandpass filtering was accomplished by using 30 commercial narrow bandpass interference filters. The spectral transmittances of the filters are shown in Fig. 3.7. The original RGB camera was replaced by a QImaging Retiga-4000RV monochrome CCD camera.

For safety reasons, it is practical that the light is filtered before it is guided into the eye. This way, one can insure that the optical power levels stay below the safety limits defined by the American National Standards Institute (ANSI, [69]) or the International Commission on Non-Ionizing Radiation Protection (ICNIRP, [70]). The interference filters were used one by one to filter the imaging light and a digital image of the ocular fundus was captured for each filter. Due to the constant involuntary movements of the eye, a set of five images were taken for each filter, and of each set only one image was manually chosen for post-processing.

*Figure 3.11: The spectral fundus camera system used in Papers **I** and **II**.*

Due to the movements of the eye, each selected spectral channel image was slightly misaligned with respect to the others. The process of setting two misaligned images of the same scene into the same coordinate system is called *image registration*. In papers **I** and **II**, fundus image registration was done by using an automatic image registration program by Stewart *et al*. [71]. The program used the generalized dual-bootstrap iterative closest point (GDB-ICP) algorithm for image registration [72]. Difficult image pairs were registered manually using MATLAB [73]. Also, the exposure times were different for each spectral channel image. Hence, in order to make the spectral channels comparable, every image was normalized into unit exposure time. From the normalized and registered spectral channel images, a $1024 \times 1024 \times 30$ spectral fundus image was constructed by stacking the images in wavelength order. Now,

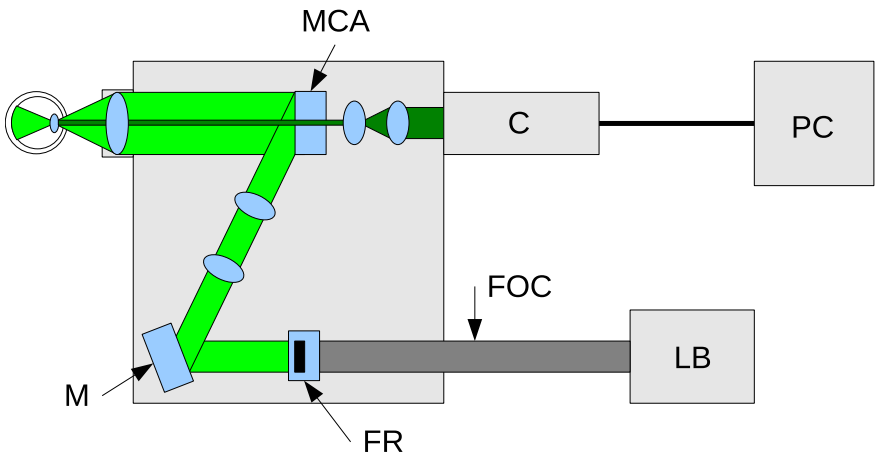

Figure 3.12: Simplified structure and operation of the spectral fundus camera system. LB: light box; FOC: fiber optic cable (liquid light guide); FR: filter rails; M: mirror; MCA: mirror with a central aperture; C: camera; PC: personal computer.

every pixel (x, y) in the spectral image contains a vector $\mathbf{v}$ according to Eq. (3.5).

A white reference spectrum (Eq. (3.6)) was acquired using the same procedure as above, but instead of an eye, the imaged object was a Spectralon-coated non-fluorescent diffuse white reflectance standard. Spectralon reflects over 99% of all wavelengths in the visual range of light. By measuring the sample, a $1024 \times 1024 \times 30$ spectral image for the white reference was obtained. The surface of the white standard is flat, whereas the fundus camera optics have been designed to distribute light evenly on a curved surface (i.e. fundus of the eye). Therefore, the white reference spectral image could not be used directly with the fundus spectral image to obtain fundus reflectance data. Instead, a mean spectrum from a 100×100 spatial area in the white reference spectral image was used as $\mathbf{v}_{\text{white}}$ of Eq. (3.6). For 8-bit spectral channel images, the average effect of dark background noise was less than 0.4%. Hence, the noise component was approximated to be zero, i.e. $\mathbf{v}_{\text{dark}} \approx 0$. From Eq. (3.7), one finds for the spectral fundus image pixel (x, y):

$$\mathbf{r} = \mathbf{T}_{\mathrm{OM}}^2 \mathbf{r}_{\mathrm{retina}} = \frac{\mathbf{v}}{\mathbf{v}_{\mathrm{white}}} , \tag{3.8}$$

where $\mathbf{T}_{\mathrm{OM}} = \mathrm{diag}(\mathbf{t}_{\mathrm{OM}})$ and $\mathbf{t}_{\mathrm{OM}}$ is the spectral transmittance of the ocular media (cornea, aqueous, lens, vitreous). Since $\mathbf{T}_{\mathrm{OM}}$ is unique for each eye and it cannot be measured *in vivo*, its effect remains in the results. Measured light passes through the ocular media twice, hence the second power in Eq. (3.8).

3.5 PARTICLE SWARM OPTIMIZATION

In Paper **II**, the weights of the illuminants' different spectral channels were optimized using particle swarm optimization (PSO) algorithm [74, 75]. The aim was to study optimal illuminants that could be used in retinal imaging to enhance the visibility of diabetic retinopathy lesions. In PSO, a swarm of N particles is randomly initiated in a solution space S. The task of the particles is to find a point $\hat{\mathbf{g}} \in S$ which minimizes or maximizes the given fitness function $f(\mathbf{x})$. During every iteration step t, each particle is aware of the best solution it has found so far (*localBest*), and of the best solution found by the entire swarm (*globalBest*). Every particle has a position vector $\mathbf{x}_i$ and a velocity vector $\mathbf{v}_i$, where $i = 1, \ldots, N$. During every iteration step t, the position and velocity are updated as follows [75]:

$$\begin{aligned} \mathbf{v}_i(t+1) \leftarrow\ & C_0 \mathbf{v}_i(t) + C_1 \mathbf{r}_1(t) \left(localBest_i(t) - \mathbf{x}_i(t)\right) \\ & + C_2 \mathbf{r}_2(t) \left(globalBest(t) - \mathbf{x}_i(t)\right) \\ \mathbf{x}_i(t+1) \leftarrow\ & \mathbf{x}_i(t) + \mathbf{v}_i(t+1) , \end{aligned} \tag{3.9}$$

where constant C_0 is called inertia, constants C_1 and C_2 determine how much weight the particle gives to the current *localBest* and *globalBest* solutions, and $\mathbf{r}_1(t)$ and $\mathbf{r}_2(t)$ are random vectors that contain values from a uniform distribution $U[0, 1]$. The PSO algorithm is described in Algorithm 1. The particles are updated until convergence and the final *globalBest* is the vector $\hat{\mathbf{g}}$. There is a

chance that $f(\hat{\mathbf{g}})$ is only a local minimum/maximum and $\hat{\mathbf{g}}$ is not the best possible solution. Using a relatively large number of particles increases the possibility of finding the optimal solution.

Algorithm 1 Particle swarm optimization algorithm.

for each iteration step t **do**
  for each particle i **do**
    calculate new position $\mathbf{x}_i$ using the formulas in Eq. (3.9)
    calculate the value of the fitness function $f(\mathbf{x}_i)$
    if $f(\mathbf{x}_i)$ is better than $f(localBest_i)$ **then**
      $localBest_i \leftarrow \mathbf{x}_i$
    end if
    if $f(\mathbf{x}_i)$ is better than $f(globalBest)$ **then**
      $globalBest \leftarrow \mathbf{x}_i$
    end if
  end for
end for

3.6 OPTICAL COHERENCE TOMOGRAPHY

Optical coherence tomography (OCT) is an optical, non-contact method for recording three-dimensional (3-D) structures from scattering media in a micrometer resolution [13,14]. The primary application for OCT has always been the imaging of biological tissue, and OCT has been successfully implemented in studies of e.g. human skin, blood vessels and gastrointestinal tissues [15,76,77]. However, ever since the birth of OCT, perhaps the main target of interest has always been the human eye and its complex multilayered structures [78–81]. In hospitals and eye clinics, commercial OCT devices are used routinely to observe the cross-sections of the retina for the detection of e.g. retinal edema, macular holes, and nerve fiber layer thickness changes. Besides biomedical imaging, OCT has been used in industrial applications, such as in the quality control of paper and printed electronics [16,17,82,83].

OCT is an interferometric method based on low-coherence interferometry [84]. In OCT, one is interested in the *reflectivity* of the sample as a function of spatial coordinates (x, y, z) inside the sample volume. For fixed coordinates (x, y) on the sample surface, the reflectivity spectrum $I(x, y, z)$ as a function of depth z (i.e. the depth profile along the optical axis) is called an A-scan. A series of adjacent A-scans along a line is called a B-scan (i.e. a 2-D cross-section of the sample volume). Logically, a series of B-scans in the orthogonal direction is called a C-scan (i.e. a 3-D volume).

A time-domain OCT (TD-OCT) system typically consists of a low-coherence light source, a free-space or a fiber optic Michelson interferometer and a detector (Fig. 3.13). A Michelson interferometer has four arms: a light source arm, a sample arm, a reference arm and a detection arm. As light reflects/backscatters from the sample and the reference mirror, and finally reaches the detector, only the interference of the photons that have an optical path length difference within the coherence length of the light source is detected. Therefore, a TD-OCT system can measure only a single point from the sample with one measurement. Depth scanning is done by mov-

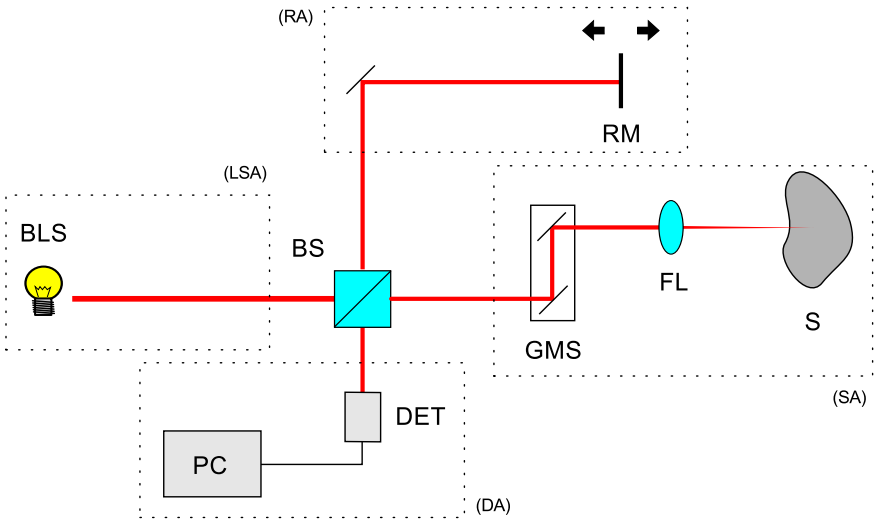

Figure 3.13: Simplified schematic of a time-domain OCT system using free-space optics. Also, the four arms of an OCT system are identified (dotted line): light source arm (LSA), reference arm (RA), sample arm (SA), and detection arm (DA). Here, BLS: broadband light source; BS: beam splitter; RM: reference mirror; GMS: galvo mirror system; FL: focusing lens; S: sample; DET: detector; PC: personal computer. Note that the reference mirror must be moved in order to do axial (depth) scanning. Lateral scanning is done by the galvo mirrors.

ing the reference mirror, i.e. by increasing or decreasing the optical path length. In order to record a full 3-D volume, one must also scan the beam in the two lateral directions. Lateral scanning can be accomplished e.g. by moving the sample or by using a galvo mirror system to scan the beam. Since every point in a 3-D volume must be measured separately, TD-OCT is a relatively slow measurement method.

Spectral-domain OCT (SD-OCT) offers useful improvements to TD-OCT: it has significantly faster measurement times and over a 100-fold increase in sensitivity [84, 85]. The basic optical setup of SD-OCT is similar to TD-OCT, except that now the detection arm contains a spectrometer (Fig. 3.14). Since most OCT systems use infrared or near-infrared light sources, single mode fibers and fiber couplers are often used to replace the free-space light distribution

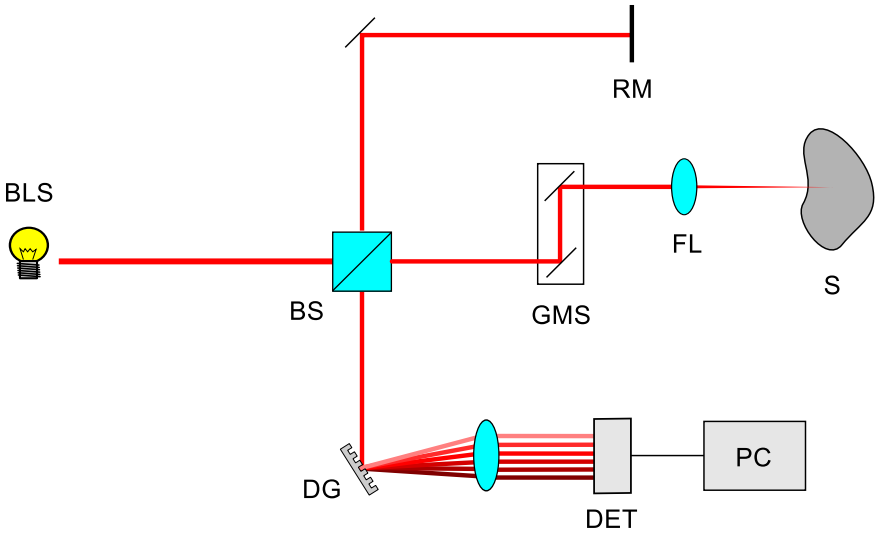

Figure 3.14: Simplified schematic of a spectral-domain OCT system using free-space optics. BLS: broadband light source; BS: beam splitter; RM: reference mirror; GMS: galvo mirror system; FL: focusing lens; S: sample; DG: diffraction grating; DET: detector; PC: personal computer. Note that the reference mirror position is fixed. Lateral scanning is done by the galvo mirrors.

optics (see Fig. 3.15). A spectrometer consists of a dispersive element, e.g. a diffraction grating, which disperses the incoming light into its spectral components, and focusing optics followed typically by a high-speed line scan detector. Now, instead of measuring an A-scan point-by-point, one obtains the full information of an A-scan with a single spectral measurement. As depth scanning is not required in SD-OCT, the reference mirror position is fixed. Only lateral scanning is needed to record a 3-D volume.

In OCT, the use of a low-coherence (i.e. broadband) light source is critical. The central wavelength λ_c and the optical bandwidth $\Delta\lambda$ of the light source used immediately affect the axial (depth) imaging resolution Δz. Assuming that the light source emission spectrum has a Gaussian shape, and that the optical bandwidth $\Delta\lambda_{\mathrm{FWHM}}$ is defined as the full width at half maximum (FWHM) of the light source spectrum, then the axial resolution is half of the coherence length of the light source ℓ_{coh}, as follows [84]:

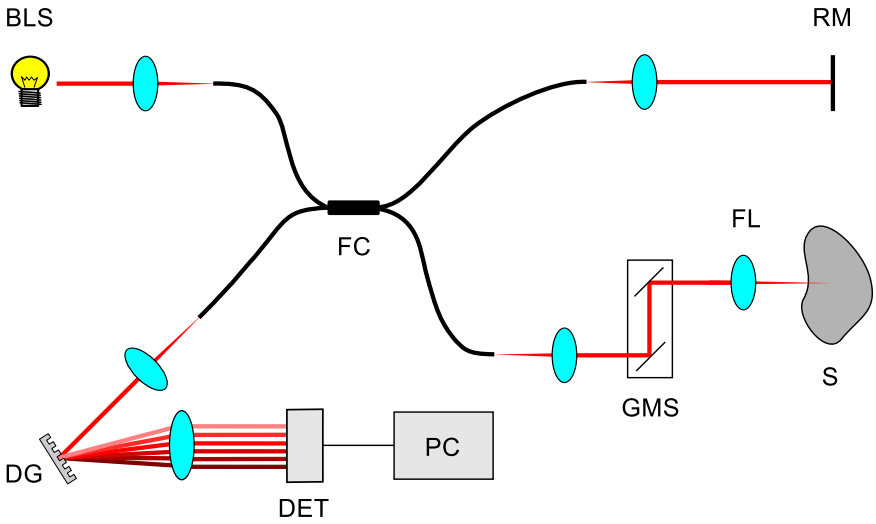

Figure 3.15: Simplified schematic of a spectral-domain OCT system using optical fibers. BLS: broadband light source; FC: fiber coupler; RM: reference mirror; GMS: galvo mirror system; FL: focusing lens; S: sample; DG: diffraction grating; DET: detector; PC: personal computer.

$$\Delta z = \frac{\ell_{\mathrm{coh}}}{2} = \frac{2\,ln(2)}{\pi n_{\mathrm{s}}} \frac{\lambda_{\mathrm{c}}^2}{\Delta\lambda_{\mathrm{FWHM}}} \,. \tag{3.10}$$

Here n_{s} is the refractive index of the sample. The axial resolution Δz depends only on the light source (and on the refractive index of the sample). In the literature, the theoretical axial resolutions are often given in air ($n_{\mathrm{air}} = 1$), and are also often estimated for the sample materials. For example, the refractive indices for some sections of the human eye are listed in Subsection 3.3.1. From Eq. (3.10) one immediately notices that higher refractive indices result in better axial imaging resolutions. As for the two lateral dimensions (along the sample surface), the imaging resolutions Δx and Δy are equal to the spot size of the focused scanning beam [84].

The depth measurement range of an SD-OCT system depends on the number of pixels in the detector array. As light reflects/back-scatters from increasingly deeper layers in the sample, the frequency of the detected interference fringes increases with depth. As the

spectrum of the interfering light is focused onto the detector array, the number of pixels the spectrum is projected upon (i.e. the spectral resolution $\delta\lambda$, nanometers/pixel) determines the highest possible frequency of an interference fringe that can still be detected. If a spectrum with a full spectral range of $\Delta\lambda$ is focused on N pixels, then the maximum detectable depth range $z_{\max}$ in the sample is [78,86]:

$$z_{\max} = \frac{1}{4n_{\mathrm{s}}} \frac{\lambda_0^2}{\Delta\lambda/N} = \frac{\lambda_0^2}{4n_{\mathrm{s}}\delta\lambda} \,, \tag{3.11}$$

where λ_0 is the central wavelength of the focused spectrum and n_{s} is the refractive index of the sample.

The spectrum of the interfering light $S(\lambda)$ is captured by the line scan detector, and this spectrum is mapped from wavelength-space to wavenumber-space (wavenumber $k = 2\pi/\lambda$). Due to the nonlinear relationship between wavelengths and wavenumbers, the k-space spectrum $S(k)$ needs to be interpolated to even spacing. The measured spectrum $S(k)$ can be written as follows [78]:

$$S(k) = I_{\mathrm{s}}(k) + I_{\mathrm{ref}}(k) + 2\sqrt{I_{\mathrm{s}}(k) I_{\mathrm{ref}}(k)} \sum_{\mathrm{n}} \alpha_{\mathrm{n}} \cos(k z_{\mathrm{n}}) \,, \tag{3.12}$$

where the first two terms $I_{\mathrm{s}}(k)$ and $I_{\mathrm{ref}}(k)$ are the measured intensities coming from the sample and the reference mirror, respectively. The third term describes the interference between the light returning from the reference mirror and the light returning from depth z_{n} in the sample. Here α_{n} is the square root of the reflectivity value at depth z_{n}.

The axial structure of the sample is gained by taking an inverse Fourier-transformation of the measured spectrum $S(k)$ [78,87]:

$$\begin{aligned} I(z) &= \mathrm{FT}^{-1}\left\{S(k)\right\} \\ &= \Gamma(z) \otimes \left(1 + \sum_{\mathrm{n}} \alpha_{\mathrm{n}} \delta(z - z_{\mathrm{n}}) + \sum_{\mathrm{n}} \alpha_{\mathrm{n}} \delta(z + z_{\mathrm{n}}) + O\left[I_{\mathrm{s}}(k)\right] \right) \,, \end{aligned} \tag{3.13}$$

where FT^{-1} denotes the inverse Fourier-transformation, $\otimes$ denotes convolution, $\Gamma(z)$ is the coherence function and $\delta(z - z_n)$ is the Dirac delta function centered at depth z_n. The first term (1; inside the brackets) describes the autocorrelation signal coming from the reference arm, and $O\left[I_s(k)\right]$ is an autocorrelation noise term resulting from interference within the sample arm. Due to the properties of the Fourier-transformation, one obtains two sum-terms $\sum_n \alpha_n \delta(z \pm z_n)$ which contain the desired reflectivity information α_n for depths z_n in the sample. These sums are the real and complex conjugate reflectivity profiles, and they are mirror-symmetric with respect to the zero optical path length difference. In order to get a depth profile (A-scan), all other terms except the real reflectivity profile are discarded. This sequence is shown in Fig. 3.16(a).

In practice, the optical elements in the arms of an OCT system cause dispersion. Dispersion is caused by the wavelength-

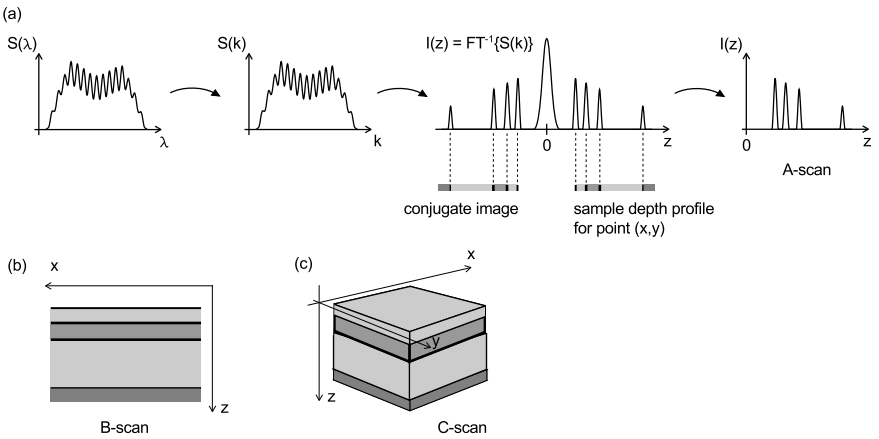

Figure 3.16: A-, B- and C-scans in spectral-domain OCT. (a) Measured spectrum $S(\lambda)$ is mapped into wavenumber-space ($k = 2\pi/\lambda$) and interpolated to constant interval. One gets function $I(z)$ as a function of depth z by taking an inverse Fourier-transformation of $S(k)$. The function $I(z)$ consists of a DC component at $z = 0$, and of real and complex conjugate images on the positive and negative sides, respectively. By taking only the real image, one gets a reflectivity spectrum as a function of depth for a single point (x, y). (b) A cross-section of the sample (B-scan). (c) A 3-D volume of the sample (C-scan). The beam propagates in the direction of the z-axis.

dependency of the optical materials' refractive indices. The presence of a dispersion mismatch between the sample and reference arms in OCT results in poor depth imaging resolution [14,88]. One can attempt to match the dispersion in the interferometer's two arms prior to measurements by e.g. adding elements of glass or fused silica to the optical system. An alternative option is to do numerical dispersion compensation in data post-processing [89].

4 Experimental studies and results

4.1 SPECTRAL IMAGING OF THE OCULAR FUNDUS

In Papers **I** and **II**, the spectral images were recorded from the ocular fundi of 72 voluntary human subjects using the spectral fundus camera system described in Section 3.4. Of the volunteers, 55 were diabetics and 17 were healthy control subjects. Fully informed consents were obtained from the volunteers prior to the measurements. The trials followed the research ethical principles of the Declaration of Helsinki and were approved by the local research ethics committee of the Hospital District of Northern Savo, Finland [90]. The diabetic patients were recruited and measured in the Department of Ophthalmology in the Kuopio University Hospital (Kuopio, Finland). The healthy volunteers were measured in the Color Research Laboratory of the University of Eastern Finland (Joensuu, Finland).

4.2 SPECTRAL FUNDUS IMAGES AND PSEUDO-COLOR IMAGES

Four example RGB representations of the recorded spectral fundus images from diabetic eyes are shown in Fig. 3.10. Figure 3.8(b) (page 16) shows an RGB representation of a spectral fundus image for one of the non-diabetic healthy control subjects. The RGB representations were calculated for the CIE (Commission Internationale de l'Eclairage) 1931 standard colorimetric observer and D_{65} standard illuminant [28].

By replacing the red, green and blue layers in an RGB image by specific spectral channel images, e.g. $I_{580nm} \rightarrow$ R, $I_{550nm} \rightarrow$ G and $I_{500nm} \rightarrow$ B, one acquires pseudo-color fundus images with better contrast and lesion visibility than in a typical RGB fundus image.

Figure 4.1: RGB-representations calculated from three diabetic spectral fundus images (left column), and pseudo-color images of the same ocular fundi using registered spectral color channels (right column). The used spectral channels in the right-hand side images are 580, 550 and 500 nm. No image processing (e.g. contrast enhancement) has been applied to any of the images.

In Fig. 4.1, images of three diabetic ocular fundi are shown in RGB and in pseudo-color. The use of specific spectral color channels increases the contrast and visibility of diabetic lesions compared to standard RGB images. The 72 measured spectral fundus images and associated diabetic lesion markings made by eye care professionals were combined into a single spectral image database.

4.3 CALCULATION OF OPTIMAL ILLUMINATIONS FOR DIABETIC RETINOPATHY LESION DETECTION

The fact that spectral reflectance data is independent of illumination or observer allows one to study the optimal spectral shapes of illuminations that would maximize the visibility of the diabetic lesions for a detector with a certain spectral sensitivity. In Paper **II**, the optimal illuminations for the detection of diabetic retinopathy lesions were calculated. These illuminations maximized the visual contrast between diabetic lesions and surrounding healthy tissue.

As it was unrealistic to assume that a single illuminant would maximize the visibility of several different kinds of diabetic lesions, the optimal spectral power distribution (SPD) of the illuminant was calculated for each lesion type separately. The optimal illuminations were calculated for the following cases: (1) microaneurysms, (2) hard exudates, (3) microinfarcts, (4) fibrosis, (5) laser photocoagulation scars and (6) blot bleedings. Also, optimal SPDs that gave (7) maximum contrast between macular and non-macular areas, and (8) maximum contrast between arteries and veins were obtained.

In Paper **II**, the contrast measure used was Michelson contrast, which is defined as follows:

$$c = \frac{max\left\{I_1, I_2\right\} - min\left\{I_1, I_2\right\}}{max\left\{I_1, I_2\right\} + min\left\{I_1, I_2\right\}} \,. \tag{4.1}$$

Here the intensity values $I_j \in [0, 1]$, $j = 1, 2$, are defined as

$$I_j = k\mathbf{s}^{\mathrm{T}}\mathbf{H}\mathbf{r}_j \,, \tag{4.2}$$

where normalization constant $k = 1/(\mathbf{s}^{\mathrm{T}}\mathbf{h})$, diagonal matrix $\mathbf{H} = \mathrm{diag}(\mathbf{h})$, and vector $\mathbf{h}$ is the spectral sensitivity of the monochrome detector. The vectors $\mathbf{r}_j$, $j = 1, 2$, are the mean reflectance spectra for a selected diabetic lesion and its surrounding healthy tissue, respectively, calculated from 3×3 pixel spatial areas. The vector $\mathbf{s}$ is the SPD of the illuminant, and is here defined as a convex combination of the narrow bandpass interference filters (Fig. 3.7):

$$\mathbf{s} = \mathbf{F}\mathbf{a} \,, \tag{4.3}$$

where matrix $\mathbf{F}$ has the spectral transmittances of the narrow bandpass interference filters on its columns, and $\mathbf{a} \in \Re^n$ is a weight vector, so that $\mathrm{a}_i \geq 0$, $i = 1, \ldots, n$, and $\sum_{i=1}^{n} \mathrm{a}_i = 1$. As the weight vector $\mathbf{a}$ is the only unknown, the SPD $\mathbf{s}$ that produces the best possible Michelson contrast value c for given reflectance spectra $\mathbf{r}_1$ and $\mathbf{r}_2$ can be obtained using the particle swarm optimization (PSO) algorithm described in Section 3.5.

The mean reflectance spectra $\mathbf{r}_1$ and $\mathbf{r}_2$ were collected from the spectral fundus images for every above-mentioned case (1)–(8) separately. In cases (1)–(4) and (6), the "diabetic lesion"/"surrounding healthy tissue" reflectance spectrum pairs were obtained from five different locations in every spectral image where the particular lesion type was present. In case (5) (laser photocoagulation scars), five "scar tissue"/"surrounding healthy tissue" reflectance spectrum pairs were selected from each applicable spectral image. Analogously, in cases (7) and (8), five "macular/ non-macular" and "artery/vein" reflectance spectrum pairs were chosen from each suitable spectral image, respectively. Then, an optimal SPD was calculated with the PSO algorithm for each collected spectrum pair separately. Finally, the optimized SPDs were gained by combining the individual results for each studied case.

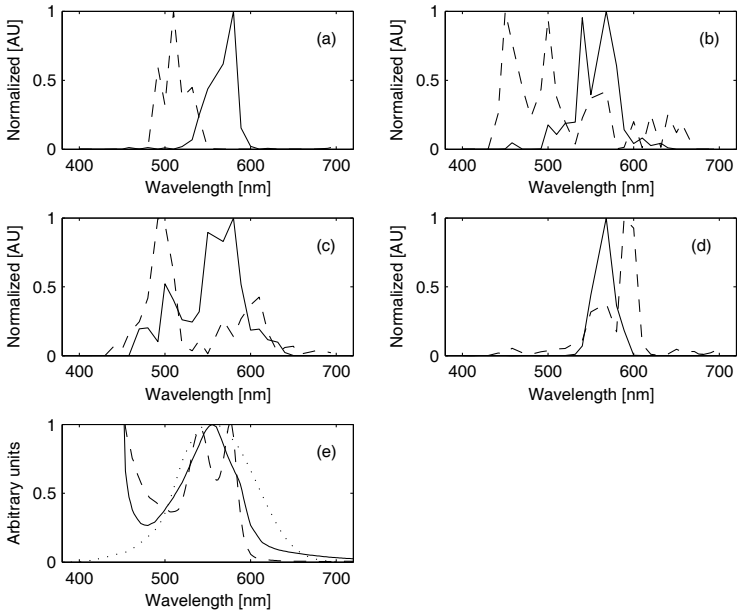

Figure 4.2: The spectral power distributions of the optimal illuminants for the detection of (a) microaneurysms (solid line), microinfarcts (dashed line), (b) hard exudates (solid line), fibrosis (dashed line), (c) laser photocoagulation scars (solid line), macula (dashed line), (d) blot bleedings (solid line), and arteries versus veins (dashed line). In (e), the photopic luminosity function (dotted line), and the absorption spectra of hemoglobin Hb (solid line) and oxyhemoglobin HbO_2 (dashed line) are shown in arbitrary units.

4.4 OPTIMAL ILLUMINATIONS AND COMPUTATIONAL EXAMPLE IMAGES

The optimized SPDs are shown in Fig. 4.2. A detailed analysis on the results obtained can be found in Paper **II**. For a single diabetic lesion/healthy tissue pair, the optimal SPD usually consists of a single narrow spectral band. The positions of these bands varied slightly as a function of wavelength between different pairs and different eyes. Certain spectral bands appeared as optimization results frequently, whereas some bands appeared rarely. These rare solutions were considered to be outliers, and were removed from the

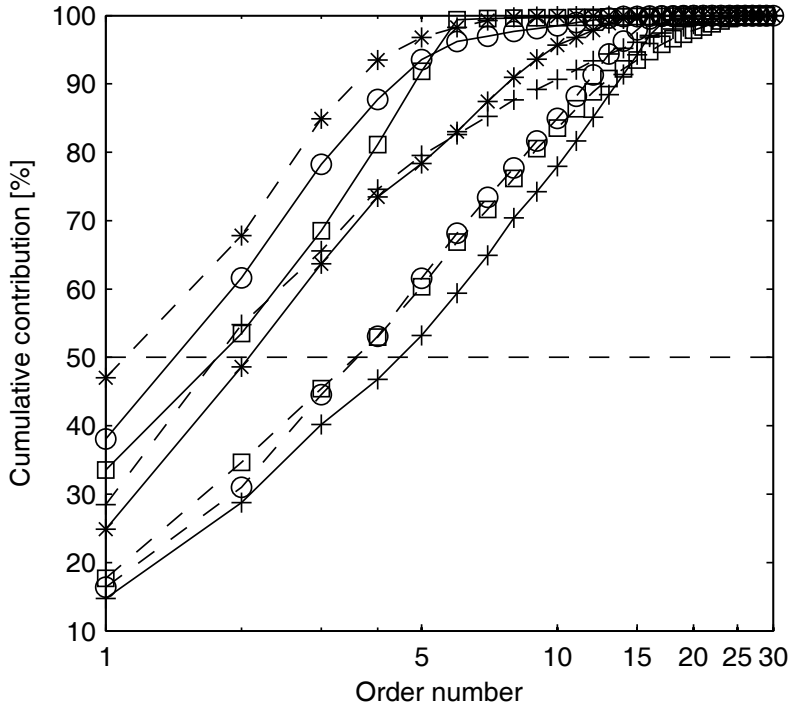

Figure 4.3: The spectral channels cumulative contribution to the SPDs of Fig. 4.2. The most significant spectral channel has the order number 1, and the least significant channel has the order number 30. Cases: microaneurysms (solid line, circles), hard exudates (solid line, asterisks), microinfarcts (solid line, squares), fibrosis (solid line, plus), laser photocoagulation scars (dashed line, circles), blot bleedings (dashed line, asterisks), macula (dashed line, squares), and arteries vs veins (dashed line, plus signs). Also, the 50% limit is presented.

SPDs in Fig. 4.2. Figure 4.3 shows the spectral channels' cumulative contributions to the gained SPDs. In the figure, order numbers 1 and 30 mean the most significant and least significant spectral channels, respectively. Only the first channels which accounted for just over 50% of the SPD were selected; the rest of the channels were considered to be outliers. For example, for microaneurysms, one needs the first two spectral channels to get $> 50\%$ cumulative contribution. The resulting outlier-free SPDs are shown in Fig. 4.4.

To visualize the effect these optimal illuminants would have in

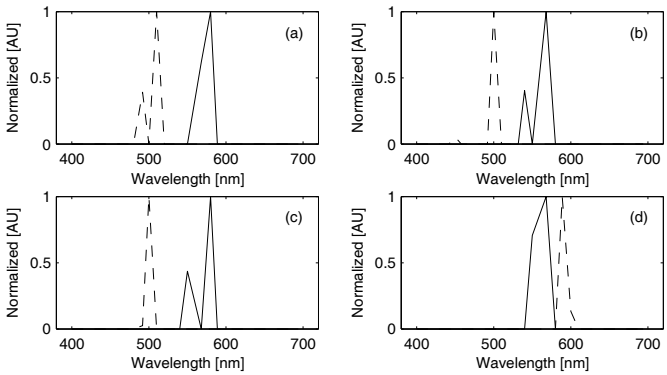

Figure 4.4: The outlier-free spectral power distributions of the optimal illuminants. (a) Microaneurysms (solid line), microinfarcts (dashed line), (b) hard exudates (solid line), fibrosis (dashed line), (c) laser photocoagulation scars (solid line), macula (dashed line), (d) blot bleedings (solid line), and arteries versus veins (dashed line).

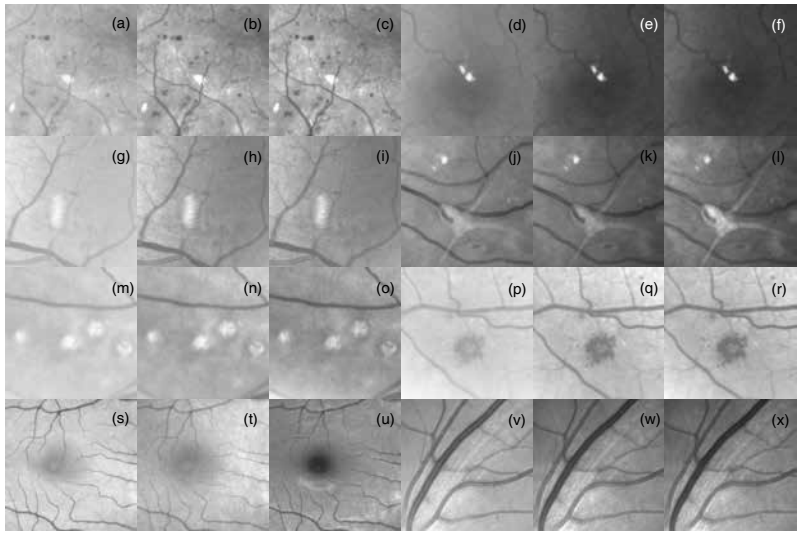

Figure 4.5: Segments from computational example images demonstrating the effect of the optimized illuminations. Left: green channel of an RGB image; center: effect of the illuminant from Fig. 4.2; right: effect of the illuminant from Fig. 4.4. Cases: (a)–(c) microaneurysms, (d)–(f) hard exudates, (g)–(i) microinfarcts, (j)–(l) fibrosis, (m)–(o) laser photocoagulation scars, (p)–(r) blot bleedings, (s)–(u) macula, and (v)–(x) arteries versus veins.

retinal imaging, computational example images were calculated. As can be seen from the computational example images in Fig. 4.5, the contrast and visibility were improved in all studied cases when compared to the green channel of an RGB image. The outlier-free SPDs are found to perform as well or even better than the original optimized SPDs. In Paper **II**, only theoretical computational examples were considered, so the performances of the optimal illuminations were not tested in clinical trials. However, the results indicate that the contrast and visibility of retinal features in fundus images could be improved simply by using a suitable illumination during the actual retinal imaging.

4.5 EFFECT OF THE COLLIMATOR LENS IN THE SAMPLE ARM OF AN OPTICAL COHERENCE TOMOGRAPHY SYSTEM

Most modern OCT systems use optical single mode fibers to distribute infrared/near-infrared light into reference and sample arms (see Fig. 3.15). In the sample arm, the first *collimator lens* after the fiber tip transforms the emerging cone of light into a collimated beam. As the magnification of the optical system after the collimator lens is typically a constant, the diameter of the collimated beam after the collimator also determines the diameter of the collimated beam that enters the eye (see Figs. 4.6(a) and 4.7(a)).

In Paper **III**, the original research hypothesis was as follows: a "long focal length" collimator lens produces a relatively wide collimated beam that enters the eye, and thus, a relatively small focused spot size on the retina (good lateral resolution). On the downside, the spot size on the fiber tip for the returning light is relatively large, and only a portion of the reflected/backscattered light actually enters the fiber core and reaches the detection arm (see Fig. 4.6). For a "short focal length" collimator lens, the situation is reversed: the collimated beam entering the eye is relatively narrow, resulting in a relatively large focused spot on the retina (poor lateral resolution). However, for the reflected light, the spot size on the fiber tip

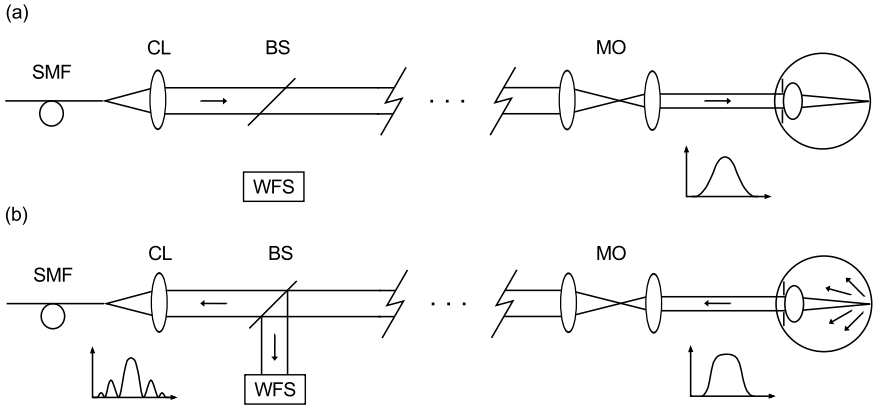

Figure 4.6: Adaptive-optics OCT sample arm with a "long focal length" collimator lens. SMF: single mode fiber; BS: beam splitter; MO: magnification optics; WFS: wavefront sensor. The cut-off contains additional optics and deformable mirrors. The subplots show the simplified beam profiles.

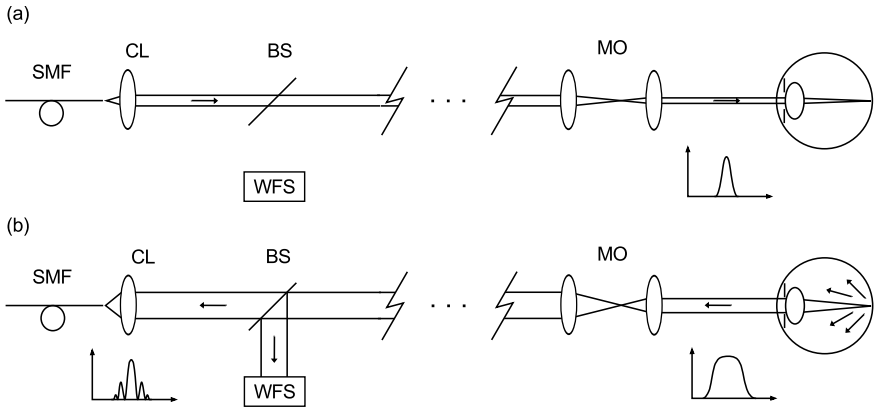

Figure 4.7: Adaptive-optics OCT sample arm with a "short focal length" collimator lens. SMF: single mode fiber; BS: beam splitter; MO: magnification optics; WFS: wavefront sensor. The cut-off contains additional optics and deformable mirrors. The subplots show the simplified beam profiles.

is relatively small, so light collection into the fiber is better than for the long focal length collimator (see Fig. 4.7).

When a wide beam (e.g. a diameter of ∼7–8 mm) is guided into the eye, the optical aberrations caused by the eye's optics de-

teriorate the wavefront so that the spot size on the retina is not diffraction limited. These aberrations can be corrected by using adaptive optics (AO). A typical AO-system consists of a wavefront sensor (WFS), which monitors the optical aberrations at the plane of the eye's pupil, and deformable mirrors which correct the detected aberrations.

In Paper **III**, the effect of the focal length of a collimator lens on the recorded B-scan image quality was studied. The AO-OCT system used has been described in detail in Refs. [24, 26, 91]. The AO-OCT system used a superluminescent diode (Superlum Ltd., Moscow, Russia) as a broadband light source (central wavelength λ_c = 840 nm and bandwidth $\Delta\lambda$ = 112 nm). A single mode fiber and a 90/10 fiber optic coupler were used to distribute the near-infrared light into reference and sample arms. In the sample arm, all the optics remained unchanged, except for the first collimator lens. The four tested collimator lenses had focal lengths of 50, 25, 18.2 and 9 mm. The 18.2 and 9 mm collimators were microscope objectives. Immediately after the collimator lenses, the collimated beams' full widths at half maximum (FWHM) were approximately 10.0, 5.0, 3.6 and 1.8 mm, respectively.

In the AO-OCT system's sample arm, the collimated beam was guided into a free-space optical system which had a constant magnification of $\sim$0.66. Hence, the collimated beams entering the eye had FWHMs of approximately 6.6, 3.3, 2.4 and 1.2 mm, respectively. B-scans were recorded from the eye of a voluntary human subject for each tested collimator lens separately. The B-scans are shown in Fig. 4.8. The ethical tenets of the Declaration of Helsinki were followed, and a fully informed consent was acquired from the subject prior to the measurements [90]. The subject's pupil was dilated with mydriatics. The optical power used in the measurements was $\sim$400 μW, well below ANSI safety limits [92]. The field-of-view in the B-scans is $\sim$3.5°, which is approximately 1 mm on the retina. Also, for each collimator lens, the detected spot distributions at the WFS were recorded (these are discussed in Paper **IV** and Section 4.6).

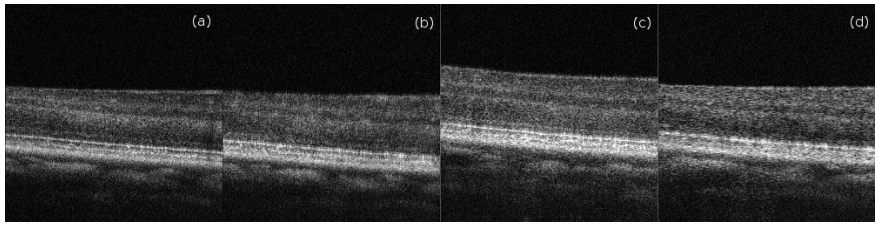

Figure 4.8: B-scans from a human retina. Collimator lens focal lengths were: (a) 50 mm, (b) 25 mm, (c) 18.2 mm, and (d) 9 mm. The diameters of the collimated beams entering the eye were approximately 6.6, 3.3, 2.4 and 1.2 mm, respectively.

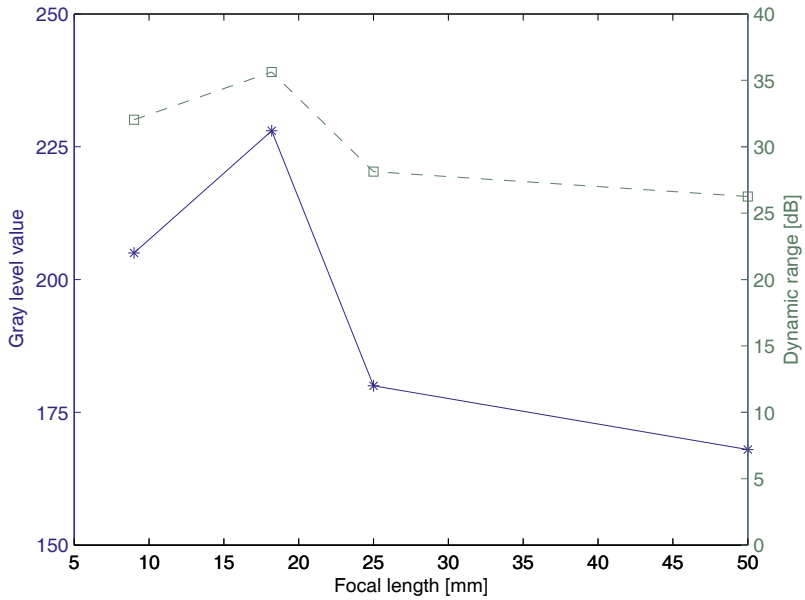

Figure 4.9: Average gray scale values and dynamic ranges of the four B-scan images in Fig. 4.8.

Figure 4.9 shows the mean gray scale values and dynamic ranges of Figs. 4.8(a)-(d). Both maximum mean gray value and maximum dynamic range were reached using the 18.2 mm focal length collimator lens. It should be noted, that the 18.2 mm and 9 mm collimators (microscope objectives) had clear apertures of only 9 mm and

6 mm, respectively, so parts of the approximately 10 mm diameter beam coming back from the eye were cut off. The increasing detected intensity with shorter focal lengths can be partially explained by the relatively narrow beams entering the eye, which then focus on the retina as a Gaussian beam with a wider beam waist and longer Rayleigh range than larger sized beams. This can be seen in the B-scan images as increased reflectivity over longer depth range and as decreased lateral resolution. In subsequent research, it was found that the variations in the detected intensity of the B-scans could be mostly explained by the optical Stiles-Crawford effect, although the spot sizes on the fiber tip undoubtedly have some effect on the amount of light that reaches the detection arm. In summary, the choice of the first collimator lens in the sample arm of an AO-OCT system affects the diameter of the beam entering the eye (entrance pupil size), spot size on the retina (lateral imaging resolution), the contribution of the optical Stiles-Crawford effect (discussed in the next section) and finally the spot size on the fiber tip for the reflected light (light collection into the fiber).

4.6 INFLUENCE OF BEAM SIZE AND SCE ON IMAGE INTENSITY IN ADAPTIVE OPTICS OPTICAL COHERENCE TOMOGRAPHY

In Paper **III**, the spot sizes on the sample arm fiber tip were assumed to cause the detected intensity variations in AO-OCT scans. However, further investigation revealed that the same intensity variations were already present in the wavefront sensor (WFS) images, before the reflected/backscattered light was focused on the fiber tip. As the optical system in the sample arm was identical for each tested collimator lens, the only plausible source for the intensity variations is the measured eye itself. Paper **IV** describes these findings.

Due to the optical Stiles-Crawford effect, the reflected/backscattered near-infrared light exiting the eye is composed of two parts: a directional component caused by the waveguiding property of

the cone photoreceptors, and a uniform component caused by non-directional scattering in the retina [52]. Gao *et al*. introduced a method to determine the contribution of the optical Stiles-Crawford effect (SCE) from Shack-Hartmann WFS images [51, 52]. In this method, a five-parameter model is fitted to a WFS spot distribution:

$$B + I \times 10^{-\rho[(x-x_0)^2+(y-y_0)^2]}\,, \tag{4.4}$$

where B is the uniform intensity offset caused by non-directional scattering in the retina, I is the peak intensity of the contribution of the optical Stiles-Crawford effect, ρ is directionality and x_0 and y_0 are lateral displacement.

WFS images were acquired for each collimator lens separately. For example, for the 50 mm focal length collimator lens, see Fig. 4.10(a). For each of the four collimators, an average WFS spot distribution was calculated by summing 10 randomly selected spots in the WFS image (e.g. Fig. 4.10(b)). The five-parameter model was then fitted to these average spot distributions using the *lsqcurvefit* function in MATLAB. The resulting parameters are shown in Fig. 4.11.

For the SCE peak intensity values I and the WFS spot mean intensity values, the coefficient of determination and the p-value were $R^2 = 0.99$ and $p = 0.004$, respectively, which indicates a statistically significant correlation. For the SCE peak intensity values I and mean intensity values of the measured B-scans, the coefficient of determination and the p-value were $R^2 = 0.92$ and $p = 0.041$, respectively, also indicating a strong correlation between the values. Hence, the optical SCE appears to explain the detected intensity variations as a function of collimator lens focal length both at the WFS and at the detector. The non-directional component of the intensity (B) is nearly a constant for all focal lengths, so it does not contribute to the detected intensity variations. Also, as described in Section 4.5, the focused spot sizes at the fiber tip limited the amount of light that entered the fiber and reached the detector. However, the optical SCE was the greatest contributor to the detected intensity variations. These results show that the choice of

the focal length of the collimator lens in the AO-OCT sample arm affects the imaging beam width (eye entrance pupil size) and therefore the directional reflection from the retina for near-infrared light. The increase in detected intensity (at the cost of lateral resolution) in retinal B-scans might be important in cases where getting a good signal from the eye is more important than image quality.

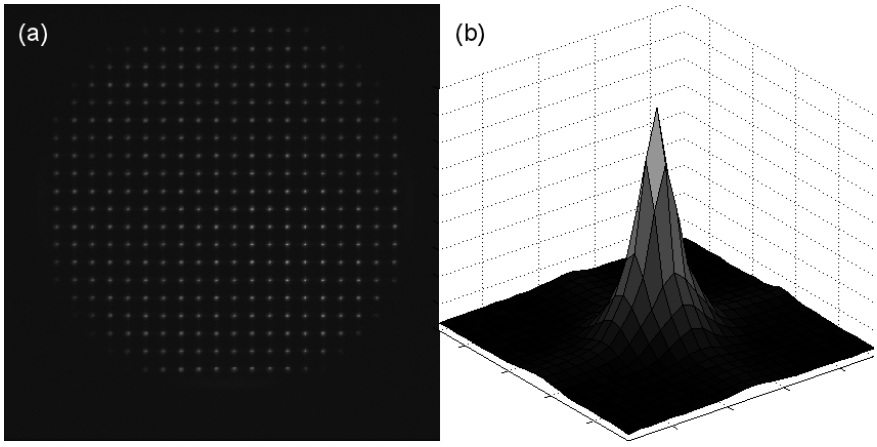

Figure 4.10: Data for 50 mm focal length collimator lens: (a) the wavefront sensor image and (b) the average WFS spot distribution.

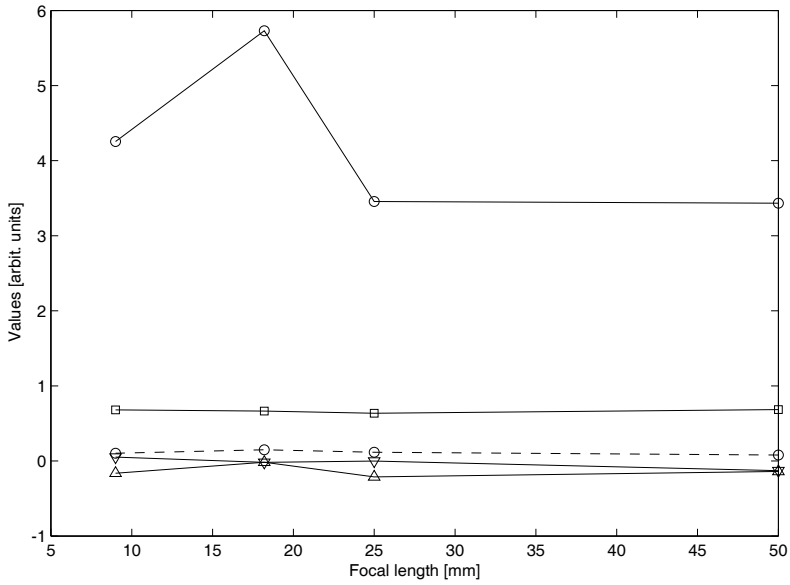

Figure 4.11: Parameters of the fitted model $B + I \times 10^{-\rho[(x-x_0)^2+(y-y_0)^2]}$ *for four collimator lenses. Parameters B (squares), I (circles),* ρ *(dashed, circles),* x_0 *(triangle up), and* y_0 *(triangle down).*

5 Discussion

The main claims in this thesis are that spectral color information can be used to enhance the visibility of diabetic retinopathy lesions and retinal landmarks in eye fundus images, spectral information can be used to calculate the spectral power distributions (SPDs) of optimal illuminations for diabetic lesion detection, and that the choice of the imaging beam width in adaptive optics optical coherence tomography (AO-OCT) affects the detected signal strength in retinal imaging.

In Papers **I** and **II**, a spectral fundus camera was constructed and 72 spectral fundus images were captured in the wavelength range of 400–700 nm with approximately 10 nm steps. The spectral imaging, using narrow bandpass interference filters (Fig. 3.7), gave high-spatial-resolution spectral images of the ocular fundus, but the imaging method was unfortunately very slow (approximately 30 min/eye). Using the acquired spectral fundus images, it was shown that narrowband spectral channel images can be combined into pseudo-color images which increase the contrast of normal and abnormal retinal features when compared to typical RGB images (Fig. 4.1). From a practical point-of-view, even though the visibility of the diabetic lesions or interesting retinal features can usually be enhanced with only a few narrow bandpass filters, capturing these images filter-by-filter in a clinical setting can be arduous and time-consuming. Therefore, automated systems should be developed for spectral filtering, such as mechanically or electronically controlled rapidly switching transmission filters for light source filtering. The use of a liquid crystal tunable filter (LCTF) is one option, although, when compared to narrow bandpass interference filters, LCTF suffers from poor light transmission especially in the violet-blue region of the visible spectrum [32]. A more ideal solution would be to use a spectrally programmable light source to generate illuminations with narrow spectral bands (e.g. a digital micromirror device based

light source, [93]), but such light sources are relatively expensive.

To prove the second claim of this thesis, the spectral fundus images were used to calculate the SPDs of the optimal illuminations which maximized the visual contrast between diabetic lesions and the surrounding healthy tissue (Figs. 4.2, 4.4 and 4.5). The optimal illuminants increased the contrast of the features of interest in all studied cases when compared to the green channel of a RGB fundus image. Traditionally, retinal image enhancements are done in post-processing, e.g. by using methods such as principal component analysis, independent component analysis or non-negative matrix factorization [94–96]. By using optimal illuminations (or narrow spectral bands for pseudo-color image formation), the visibility of retinal features could be enhanced during imaging. It should be noted that the example images in Paper **II** are computational examples of the effect that the optimal illuminants would have in the imaging of diabetic retinas. Clinical trials for testing the illuminants in practice have not been considered in this thesis and remain future work.

As for the final claim in this thesis, it was shown in Papers **III** and **IV** that the choice of the focal length of the first collimator lens in the sample arm of an AO-OCT system affects the strength of the detected signal coming from the human retina. The focal length of the collimator lens determined the eye entrance pupil size, and hence the lateral imaging resolution and the strength of the optical Stiles-Crawford effect (directional reflection from the retina), as well as the size of the focused spot on the fiber tip, potentially limiting the amount of light reaching the detection arm. At the time of writing, practically all AO-OCT systems are laboratory instruments and changing the collimator in such systems is a relatively trivial task. In the future, any commercial AO-OCT device would require, e.g., a mechanical device that swaps between "long focal length" and "short focal length" collimator lenses as needed. With an optimal choice of the collimator lenses, a balance can be found between lateral imaging resolution and detected intensity in AO-OCT scans. This might be of practical importance in cases where the measure-

ment signal is weakened by the condition of the eye or the retina (especially with elderly people).

The main challenges in the thesis work were as follows: the spectral fundus camera system produced images from relatively large areas of the ocular fundus with high spatial resolution. However, due to the manually operated light-filtering setup, the imaging of the full filter set was very time-consuming ($\sim$30 mins). This caused some strain for the human subjects as they had to stay in the same position for long periods of time. The time-consumption also limited the number of patients that could be imaged during one day.

Due to the autonomous movements of the eye, the captured spectral channel images were spatially displaced with respect to each other. Image registration set the images in the same coordinate system, but unavoidably left non-overlapping areas at the edges of the spectral images (for example, see the edges of the fundus images in Fig. 4.1). However, the non-overlapping areas are relatively small compared to the overlapping areas due to careful measurement setup. During imaging, the spectral channel images were captured with as similar fundus locations and orientations as possible. Due to the movements of the eye during spectral imaging, the spatial distributions of the illumination on the retina differ from image to image. This can have an effect on the fundus reflectance spectra, as discussed by Everdell *et al*. [68]. In the scope of this thesis, the uneven illumination in the spectral fundus images was not corrected for. However, in Paper **II**, the optimal SPDs of the illuminants were calculated from a relatively large number of reflectance spectrum pairs taken from several different eyes, so the results can be considered statistically reliable.

In AO-OCT imaging, the main challenge was the fact that data from only one human subject was available at the time of study. The test subject didn't suffer from any medical conditions that could have influenced the results. The detected intensity variations as a function of imaging beam size were a result of normal optical behavior of the human eye. Gao *et al*. have shown the validity of

the analysis method used (Refs. [51,52]), and as similar changes in intensity were detected both at the WFS and at the detector, the optical Stiles-Crawford effect becomes a plausible explanation for the observed phenomenon.

In the future, spectral cameras and other devices exploiting multispectral information may become standard tools in clinical environments. But this requires that spectral imaging devices must be able to capture spectral data faster than currently available systems. Snapshot spectral imaging would be ideal if the technology can be extended to cover relatively large spatial areas with fine spatial and spectral resolutions. The currently existing snapshot spectral imaging systems have relatively limited spatial resolutions (i.e. 350×350 pixels or less, [60,96,97]). Development of spectrally programmable light sources with fast switching times and high output power would be useful in all applications requiring spectral imaging or illumination with a predefined spectral power distribution. In most cases, cost-effectiveness is the limiting factor when it comes to translating modern optical methods into actual clinical use. The optical methods introduced in this thesis are relatively straightforward and can potentially be implemented in existing retinal imaging systems.

As future work, both the spectral fundus imaging and the AO-OCT devices/methods of this thesis could be implemented in studies of various diseases and medical conditions that affect the ocular fundus, e.g. age-related macular degeneration, glaucoma, macular edema, retinitis pigmentosa, choroidal nevus/melanoma and retinal detachment.

References

[1] W. F. Hoyt, L. Frisén, and N. M. Newman, "Fundoscopy of nerve fiber layer defects in glaucoma," *Invest. Ophthalmol. Vis. Sci.* **12,** 814–829 (1973).

[2] A. C. Bird, N. M. Bressler, S. B. Bressler, I. H. Chisholm, G. Coscas, M. D. Davis, P. T. V. M. de Jong, C. C. W. Klaver, B. E. K. Klein, R. Klein, P. Mitchell, J. P. Sarks, S. H. Sarks, G. Soubrane, H. R. Taylor, and J. R. Vingerling, "An international classification and grading system for age-related maculopathy and age-related macular degeneration," *Surv. Ophthalmol.* **39,** 367–374 (1995).

[3] J. A. Khawly, J. D. Matthews, and R. Machemer, "Appearance and rapid growth of retinal tumor (reactive astrocytic hyperplasia?)," *Graefes Arch. Clin. Exp. Ophthalmol.* **237,** 78–81 (1999).

[4] W. E. Dandy, "Intracranial pressure without brain tumor: diagnosis and treatment," *Ann. Surg.* **106,** 492–513 (1937).

[5] M. Wall, "Idiopathic intracranial hypertension," *Neurol. Clin.* **28,** 593–617 (2010).

[6] K. Kaarniranta and I. Sorri, "Diabeteksen aiheuttamat silmämuutokset," *Finnish Medical Journal* **63,** 621–624 (2008), *Diabetes-related changes in the eye*, published in Finnish.

[7] T. W. Gardner, D. A. Antonetti, A. J. Barber, K. F. LaNoue, and S. W. Levison, "Diabetic retinopathy: more than meets the eye," *Surv. Ophthalmol.* **47,** S253–S262 (2002).

[8] K. G. M. M. Alberti and P. Z. Zimmet, "Definition, diagnosis and classification of diabetes mellitus and its complications. Part 1: diagnosis and classification of diabetes mellitus. Provisional report of a WHO Consultation," *Diabet. Med.* **15,** 539–553 (1998).

[9] J. W. Anderson, C. W. C. Kendall, and D. J. A. Jenkins, "Importance of weight management in Type 2 diabetes: review with meta-analysis of clinical studies," *J. Am. Coll. Nutr. vol. no.* **22,** 331–339 (2003).

[10] T. Jarvala, J. Raitanen, and P. Rissanen, "Diabeteksen kustannukset Suomessa 1998–2007," (2010), *The costs of diabetes in Finland 1998–2007*, published in Finnish, the Finnish National Diabetes Prevention and Treatment Development Program DEHKO.

[11] http://www.kaypahoito.fi/web/kh/suositukset/naytaartikkeli/tunnus/hoi50056 (valid August 7, 2012), Current Care recommendation for prevention, diagnosis and treatment of diabetes, published in Finnish, Finnish Medical Society Duodecim.

[12] S. Tominaga, "Spectral imaging by a multichannel camera," *J. Electron. Imaging* **8,** 332–341 (1999).

[13] D. Huang, E. A. Swanson, C. P. Lin, J. S. Schuman, W. G. Stinson, W. Chang, M. R. Hee, T. Flotte, K. Gregory, C. A. Puliafito, and J. G. Fujimoto, "Optical coherence tomography," *Science* **254,** 1178–1181 (1991).

[14] A. F. Fercher, W. Drexler, C. K. Hitzenberger, and T. Lasser, "Optical coherence tomography - principles and applications," *Rep. Prog. Phys.* **66,** 239–303 (2003).

[15] A. M. Zysk, F. T. Nguyen, A. L. Oldenburg, D. L. Marks, and S. A. Boppart, "Optical coherence tomography: a review of clinical development from bench to bedside," *J. Biomed. Opt.* **12,** 051403–1–051403–21 (2007).

[16] E. Alarousu, *Low coherence interferometry and optical coherence tomography in paper measurements*, PhD thesis (University of Oulu, Finland, 2006).

[17] T. Prykäri, E. Alarousu, J. Kuivaniemi, J. Czajkowski, and R. Myllylä, "Ultra-high resolution optical coherence tomog-

raphy in paper characterization," in *Proc. OSAV'2008, The 2nd int. topical meeting on optical sensing and artificial vision* (2008), pp. 111–117.

[18] B. W. Colston, Jr., U. S. Sathyam, L. B. DaSilva, M. J. Everett, P. Stroeve, and L. L. Otis, "Dental OCT," *Opt. Express* **3,** 230–238 (1998).

[19] Y. Hori, Y. Yasuno, S. Sakai, M. Matsumoto, T. Sugawara, V. Madjarova, M. Yamanari, S. Makita, T. Yasui, T. Araki, M. Itoh, and T. Yatagai, "Automatic characterization and segmentation of human skin using three-dimensional optical coherence tomography," *Opt. Express* **14,** 1862–1877 (2006).

[20] Y. Yasuno, V. D. Madjarova, S. Makita, M. Akiba, A. Morosawa, C. Chong, T. Sakai, K.-P. Chan, M. Itoh, and T. Yatagai, "Three-dimensional and high-speed swept-source optical coherence tomography for in vivo investigation of human anterior eye segments," *Optics Express* **13,** 10652–10664 (2005).

[21] B. Cense, T. C. Chen, B. H. Park, M. C. Pierce, and J. F. de Boer, "In vivo depth-resolved birefringence measurements of the human retinal nerve fiber layer by polarization-sensitive optical coherence tomography," *Opt. Lett.* **27,** 1610–1612 (2002).

[22] B. Cense, N. A. Nassif, T. C. Chen, M. C. Pierce, S.-H. Yun, B. H. Park, B. E. Bouma, G. J. Tearney, and J. F. de Boer, "Ultrahigh-resolution high-speed retinal imaging using spectral-domain optical coherence tomography," *Opt. Express* **12,** 2435–2447 (2004).

[23] B. Cense, W. Gao, J. M. Brown, S. M. Jones, R. S. Jonnal, M. Mujat, B. H. Park, J. F. de Boer, and D. T. Miller, "Retinal imaging with polarization-sensitive optical coherence tomography and adaptive optics," *Opt. Express* **17,** 21634–21651 (2009).

[24] R. J. Zawadzki, S. M. Jones, S. S. Olivier, M. Zhao, B. A. Bower, J. A. Izatt, S. Choi, S. Laut, and J. S. Werner, "Adaptive-optics

optical coherence tomography for high-resolution and high-speed 3D retinal in vivo imaging," *Opt. Express* **13,** 8532–8546 (2005).

[25] Y. Zhang, J. Rha, R. S. Jonnal, and D. T. Miller, "Adaptive optics parallel spectral domain optical coherence tomography for imaging the living retina," *Opt. Express* **13,** 4792–4811 (2005).

[26] R. J. Zawadzki, S. S. Choi, S. M. Jones, S. S. Oliver, and J. S. Werner, "Adaptive optics-optical coherence tomography: optimizing visualization of microscopic retinal structures in three dimensions," *J. Opt. Soc. Am. A* **24,** 1373–1383 (2007).

[27] K. Kurokawa, K. Sasaki, S. Makita, M. Yamanari, B. Cense, and Y. Yasuno, "Simultaneous high-resolution retinal imaging and high-penetration choroidal imaging by one-micrometer adaptive optics optical coherence tomography," *Opt. Express* **18,** 8515–8527 (2010).

[28] G. Wyszecki and W. S. Stiles, *Color science: concepts and methods, quantitative data and formulae*, 2 ed. (John Wiley & Sons, Inc., New York, 1982).

[29] R. J. D. Tilley, *Colour and the optical properties of materials* (John Wiley & Sons, Ltd, Chichester, UK, 2000).

[30] Y. Miyake and K. Miyata, "Evaluation of multispectral imaging," in *Colour image science: exploiting digital media*, L. W. MacDonald and M. R. Luo, eds. (John Wiley & Sons, Ltd, 2002), pp. 77–97.

[31] http://www.specim.fi (valid August 7, 2012), Spectral Imaging Ltd. (Oulu, Finland).

[32] J. Y. Hardeberg, F. Schmitt, and H. Brettel, "Multispectral color image capture using a liquid crystal tunable filter," *Opt. Eng.* **41,** 2532–2548 (2002).

[33] N. Gupta, R. Dahmani, and S. Choy, "Acousto-optic tunable filter based visible- to near-infrared spectropolarimetric imager," *Opt. Eng.* **41,** 1033–1038 (2002).

[34] H.-C. Lee, *Introduction to color imaging science* (Cambridge University Press, Cambridge, UK, 2009).

[35] H. F. Edelhouser, J. L. Ubels, and C. Hejny, "The cornea and the sclera," in *Adler's physiology of the eye – 10th ed.*, P. L. Kaufman and A. Alm, eds. (Mosby, Inc., 2003), pp. 47–114.

[36] H.-L. Liou and N. A. Brennan, "Anatomically accurate, finite model eye for optical modeling," *J. Opt. Soc. Am. A* **14,** 1684–1695 (1997).

[37] S. R. Uhlhorn, D. Borja, F. Manns, and J. M. Parel, "Refractive index measurement of the isolated crystalline lens using optical coherence tomography," *Vision Res.* **48,** 2732–2738 (2008).

[38] H. Lund-Andersen and B. Sander, "The vitreous," in *Adler's physiology of the eye – 10th ed.*, P. L. Kaufman and A. Alm, eds. (Mosby, Inc., 2003), pp. 293–316.

[39] http://commons.wikimedia.org/wiki/File:Schematic_diagram_of_the_human_eye_en.svg (valid August 7, 2012), Author: Rhcastilhos, license: public domain.

[40] D. R. Williams, "Visual consequences of the foveal pit," *Inv. Ophthalmol. Vis. Sci.* **19,** 653–667 (1980).

[41] W. Drexler, U. Morgner, R. K. Ghanta, F. X. Kärtner, J. S. Schuman, and J. G. Fujimoto, "Ultrahigh-resolution ophthalmic optical coherence tomography," *Nat. Med.* **7,** 502–507 (2001).

[42] N. Nassif, B. Cense, B. H. Park, S. H. Yun, T. C. Chen, B. E. Bouma, G. J. Tearney, and J. F. de Boer, "*In vivo* human retinal imaging by ultrahigh-speed spectral domain optical coherence tomography," *Opt. Lett.* **29,** 480–482 (2004).

[43] R. K. Sharma and B. E. J. Ehinger, "Development and structure of the retina," in *Adler's physiology of the eye – 10th ed.*, P. L. Kaufman and A. Alm, eds. (Mosby, Inc., 2003), pp. 319–347.

[44] J. J. Weiter, F. C. Delori, G. L. Wing, and K. A. Fitch, "Retinal pigment epithelial lipofuscin and melanin and choroidal melanin in human eyes," *Invest. Ophthalmol. Vis. Sci.* **27,** 145–152 (1986).

[45] B.-L. L. Seagle, K. A. Rezai, Y. Kobori, E. M. Gasyna, K. A. Rezaei, and J. R. Norris, Jr., "Melanin photoprotection in the human retinal pigment epithelium and its correlation with light-induced cell apoptosis," *Proc. Natl. Acad. Sci. USA* **102,** 8978–8983 (2005).

[46] I. B. Styles, A. Calcagni, E. Claridge, F. Orihuela-Espina, and J. M. Gibson, "Quantitative analysis of multi-spectral fundus images," *Med. Image Anal.* **10,** 578–597 (2006).

[47] S. E. Palmer, *Vision science: photons to phenomenology* (MIT Press, Cambridge, Massachusetts, 1999).

[48] W. S. Stiles and B. H. Crawford, "The luminous efficiency of rays entering the eye pupil at different points," *Proc. R. Soc. Lond. B* **112,** 428–450 (1933).

[49] G. Westheimer, "Directional sensitivity of the retina: 75 years of Stiles-Crawford effect," *Proc. R. Soc. B* **275,** 2777–2786 (2008).

[50] G. Westheimer, "Entoptic phenomena," in *Adler's physiology of the eye – 10th ed.*, P. L. Kaufman and A. Alm, eds. (Mosby, Inc., 2003), pp. 441–452.

[51] W. Gao, B. Cense, Y. Zhang, R. S. Jonnal, and D. T. Miller, "Measuring retinal contributions to the optical Stiles-Crawford effect with optical coherence tomography," *Opt. Express* **16,** 6486–6501 (2008).

[52] W. Gao, R. S. Jonnal, B. Cense, O. P. Kocaoglu, Q. Wang, and D. T. Miller, "Measuring directionality of the retinal reflection with a Shack-Hartmann wavefront sensor," *Opt. Express* **17,** 23085–23097 (2009).

[53] T. Kauppi, *Eye fundus image analysis for automatic detection of diabetic retinopathy*, PhD thesis (Lappeenranta University of Technology, Finland, 2010).

[54] N. J. Wade, "Image, eye, and retina (invited review)," *J. Opt. Soc. Am. A* **24,** 1229–1249 (2007).

[55] F. C. Delori, E. S. Gragoudas, R. Francisco, and R. C. Pruett, "Monochromatic ophthalmoscopy and fundus photography," *Arch. Ophthalmol.* **95,** 861–868 (1977).

[56] D. J. Faulkner and C. M. Kemp, "Human rhodopsin measurement using a T.V.-based imaging fundus reflectometer," *Vision Res.* **24,** 221–231 (1984).

[57] J. M. Beach, K. J. Schwenzer, S. Srinivas, D. Kim, and J. S. Tiedeman, "Oximetry of retinal vessels by dual-wavelength imaging: calibration and influence of pigmentation," *J. Appl. Physiol.* **86,** 748–758 (1999).

[58] J. C. Ramella-Roman, S. A. Mathews, H. Kandimalla, A. Nabili, D. D. Duncan, S. A. D'Anna, S. M. Shah, and Q. D. Nguyen, "Measurement of oxygen saturation in the retina with a spectroscopic sensitive multi aperture camera," *Opt. Express* **16,** 6170–6182 (2008).

[59] R. A. Bone, B. Brener, and J. C. Gibert, "Macular pigment, photopigments and melanin: Distributions in young subjects determined by four-wavelength reflectometry," *Vision Res.* **47,** 3259–3268 (2007).

[60] W. R. Johnson, D. W. Wilson, W. Fink, M. Humayun, and G. Bearman, "Snapshot hyperspectral imaging in ophthalmology," *J. Biomed. Opt.* **12,** 014036 (2007).

[61] B. Khoobehi, J. M. Beach, and H. Kawano, "Hyperspectral imaging for measurement of oxygen saturation in the optic nerve head," *Invest. Ophthalmol. Vis. Sci.* **45,** 1464–1472 (2004).

[62] F. C. Delori, "Spectrophotometer for noninvasive measurement of intrinsic fluorescence and reflectance of the ocular fundus," *Appl. Opt.* **33,** 7439–7452 (1994).

[63] F. C. Delori and S. A. Burns, "Fundus reflectance and the measurement of crystalline lens density," *J. Opt. Soc. Am. A* **13,** 215–226 (1996).

[64] M. Hammer and D. Schweitzer, "Quantitative reflection spectroscopy at the human ocular fundus," *Phys. Med. Biol.* **47,** 179–191 (2002).

[65] M. Hammer, D. Schweitzer, L. Leistritz, M. Scibor, K.-H. Donnerhacke, and J. Strobel, "Imaging spectroscopy of the human ocular fundus in vivo," *J. Biomed. Opt.* **2,** 418–425 (1997).

[66] F. C. Delori and K. P. Pflibsen, "Spectral reflectance of the human ocular fundus," *Appl. Opt.* **28,** 1061–1077 (1989).

[67] D. V. Norren and L. F. Tiemeijer, "Spectral reflectance of the human eye," *Vision Res.* **26,** 313–320 (1986).

[68] N. L. Everdell, I. B. Styles, A. Calcagni, J. Gibson, J. Hebden, and E. Claridge, "Multispectral imaging of the ocular fundus using light emitting diode illumination," *Rev. Sci. Instrum.* **81,** 093706–1–093706–9 (2010).

[69] F. C. Delori, R. H. Webb, and D. H. Sliney, "Maximum permissible exposures for ocular safety (ANSI 2000), with emphasis on ophthalmic devices," *J. Opt. Soc. Am. A* **24,** 1250–1265 (2007).

[70] D. Sliney, D. Aron-Rosa, F. DeLori, F. Fankhauser, R. Landry, M. Mainster, J. Marshall, B. Rassow, B. Stuck, S. Trokel, T. M. West, and M. Wolffe, "Adjustment of guidelines for exposure

of the eye to optical radiation from ocular instruments: statement from a task group of the International Commission on Non-Ionizing Radiation Protection (ICNIRP)," *Appl. Opt.* **44,** 2162–2176 (2005).

[71] G. Yang, C. V. Stewart, M. Sofka, and C.-L. Tsai, "Registration of challenging image pairs: initialization, estimation and decision," *IEEE Trans. Pattern Anal. Mach. Intell.* **29,** 1973–1989 (2007).

[72] C. V. Stewart, C.-L. Tsai, and B. Roysam, "The dual-bootstrap iterative closest point algorithm with application to retinal image registration," *IEEE Trans. Med. Imag.* **22,** 1379–1394 (2003).

[73] http://www.mathworks.com/matlab (valid August 7, 2012), MATLAB: MATrix LABoratory, The MathWorks, Inc.

[74] J. Kennedy and R. Eberhart, "Particle swarm optimization," in *Proceedings of the IEEE international conference on neural networks* (IEEE, 1995), pp. 1942–1948.

[75] D. Bratton and J. Kennedy, "Defining a standard for particle swarm optimization," in *Proceedings of the IEEE swarm intelligence symposium* (IEEE, 2007), pp. 120–127.

[76] J. Welzel, E. Lankenau, R. Birngruber, and R. Engelhardt, "Optical coherence tomography of the human skin," *J. Am. Acad. Dermatol.* **37,** 958–963 (1997).

[77] Y. Chen, A. D. Aguirre, P.-L. Hsiung, S.-W. Huang, H. Mashimo, J. M. Schmitt, and J. G. Fujimoto, "Effects of axial resolution improvement on optical coherence tomography (OCT) imaging of gastrointestinal tissues," *Opt. Express* **16,** 2469–2485 (2008).

[78] B. Cense, *Optical coherence tomography for retinal imaging*, PhD thesis (University of Twente, the Netherlands, 2005).

[79] W. Drexler, "Cellular and functional optical coherence tomography of the human retina," *Invest. Ophthalmol. Vis. Sci.* **48** (2007).

[80] J. Jungwirth, B. Baumann, M. Pircher, E. Götzinger, and C. K. Hitzenberger, "Imaging of the whole anterior eye segment with full-range complex spectral domain optical coherence tomography," in *Optical coherence tomography and coherence techniques IV*, Vol. 7372 (SPIE-OSA, 2009), pp. 73721O–1–73721O–7.

[81] N. Nassif, B. Cense, B. H. Park, S. H. Yun, T. C. Chen, B. E. Bouma, G. J. Tearney, and J. F. de Boer, "In vivo human retinal imaging by ultrahigh-speed spectral domain optical coherence tomography," *Opt. Lett.* **29,** 480–482 (2004).

[82] J. Czajkowski, T. Prykari, E. Alarousu, J. Palosaari, and R. Myllyla, "Optical coherence tomography as a method of quality inspection for printed electronics products," *Opt. Rev.* **17,** 257–262 (2010).

[83] T. Fabritius, R. Myllylä, S. Makita, and Y. Yasuno, "Wettability characterization method based on optical coherence tomography imaging," *Opt. Express* **18,** 22859–22866 (2010).

[84] M. Wojtkowski, "High-speed optical coherence tomography: basics and applications," *Appl. Opt.* **49,** D30–D61 (2010).

[85] R. Leitgeb, C. K. Hitzenberger, and A. F. Fercher, "Performance of fourier domain vs. time domain optical coherence tomography," *Opt. Express* **11,** 889–894 (2003).

[86] M. Wojtkowski, R. Leitgeb, A. Kowalczyk, T. Bajraszewski, and A. F. Fercher, "In vivo human retinal imaging by Fourier domain optical coherence tomography," *J. Biomed. Opt.* **7,** 457–463 (2002).

[87] N. A. Nassif, B. Cense, B. H. Park, M. C. Pierce, S. H. Yun, B. E. Bouma, G. J. Tearney, T. C. Chen, and J. F. de Boer, "In vivo high-resolution video-rate spectral-domain optical coherence

tomography of the human retina and optic nerve," *Opt. Express* **12,** 367–376 (2004).

[88] M. Wojtkowski, V. J. Srinivasan, T. H. Ko, J. G. Fujimoto, A. Kowalczyk, and J. S. Duker, "Ultrahigh-resolution, high-speed, Fourier domain optical coherence tomography and methods for dispersion compensation," *Opt. Express* **12,** 2404–2422 (2004).

[89] M. Mujat, B. H. Park, B. Cense, T. C. Chen, and J. F. de Boer, "Autocalibration of spectral-domain optical coherence tomography spectrometers for in vivo quantitative retinal nerve fiber layer birefringence determination," *J. Biomed. Opt.* **12,** 041205 (2007).

[90] http://www.wma.net/en/30publications/10policies/b3 (valid August 7, 2012), Declaration of Helsinki – ethical principles for medical research involving human subjects, World Medical Association (WMA).

[91] R. J. Zawadzki, B. Cense, Y. Zhang, S. S. Choi, D. T. Miller, and J. S. Werner, "Ultrahigh-resolution optical coherence tomography with monochromatic and chromatic aberration correction," *Opt. Express* **16,** 8126–8143 (2008).

[92] ANSI, "American national standard for the safe use of lasers, ANSI Z136.1," (2000), (Laser Institute of America, Orlando, FL, USA).

[93] A. Y. Fong, "Application of digital micromirror devices for spectral response characterization of solar cells and photovoltaics," *Proc. SPIE Photonics West 2010 MOEMs-MEMs, emerging DMD-based systems and applications*, M. R. Douglass and L. J. Hornbeck, Editors, Proc. SPIE 7596, 7596-16 (2010).

[94] C. Sinthanayothin, J. F. Boyce, H. L. Cook, and T. H. Williamson, "Automated localisation of the optic disc, fovea, and retinal blood vessels from digital colour fundus images," *Br. J. Ophthalmol.* **83,** 902–910 (1999).

[95] A. F. M. Hani and H. A. Nugroho, "Retinal vasculature enhancement using independent component analysis," *J. Biomed. Sci. Eng.* **2,** 543–549 (2009).

[96] N. Lee, J. Wielaard, A. A. Fawzi, P. Sajda, A. F. Laine, G. Martin, M. S. Humayun, and R. T. Smith, "In vivo snapshot hyperspectral image analysis of age-related macular degeneration," in *Engineering in Medicine and Biology Society (EMBC), 2010 Annual International Conference of the IEEE* (IEEE, 2010), pp. 5363–5366.

[97] L. Gao, R. T. Smith, and T. S. Tkaczyk, "Snapshot hyperspectral retinal camera with the Image Mapping Spectrometer (IMS)," *Biomed. Opt. Express* **3,** 48–54 (2011).

Pauli Fält

Modern optical methods for retinal imaging

This thesis contains studies on the imaging of the human retina. Multispectral imaging and optical coherence tomography (OCT) are discussed. By using spectral color information, the visibility of retinal lesions caused by diabetes can be enhanced. For improved detection of diabetic lesions, optimal spectral light sources are computed. By choosing the imaging beam width correctly in adaptive optics OCT, detected signal strength can be improved for retinal imaging.

UNIVERSITY OF
EASTERN FINLAND

Publications of the University of Eastern Finland
Dissertations in Forestry and Natural Sciences

ISBN: 978-952-61-0868-1 (printed)
ISSNL: 1798-5668
ISSN: 1798-5668
ISBN: 978-952-61-0869-8 (pdf)
ISSNL: 1798-5668
ISSN: 1798-5676